MAXIME JUTRAS

IMPROVEMENT OF THE CHARACTERISATION METHOD OF THE JOHNSON-COOK MODEL

Mémoire présenté
à la Faculté des études supérieures de l'Université Laval
dans le cadre du programme de maîtrise Maîtrise en génie mécanique
pour l'obtention du grade de Maître ès Sciences (M.Sc.)

FACULTÉ DES SCIENCES ET DE GÉNIE
UNIVERSITÉ LAVAL
QUÉBEC

2008

Abstract

This Master of Science thesis is realized for the Defence Research and Development for Canada (DRDC) Valcartier. In a military context, the capacity to characterise independently the material for numerical simulation is important for three reasons. First, the material used are not widely used as aeronautical and car industries material. Secondly, the material parameters militarily relevant are rarely published. Thirdly, the used of secretly developed alloys could prevent from its characterisation by an external entity. The aim of the present study is to allow the DRDC Valcartier to self-characterize ductile metals for their simulation with the model Johnson-Cook, proposed in [1] and [2]. To get to this point, the Johnson-Cook model is presented starting from the CDM theory. The characterization method proposed by Johnson and Cook in [1] and [2] is introduced. Then, the experimental tests and equipments are described. After what, the work is focused on the static parameters (A, B, n, D1, D2, and D3), since those parameters are predominant compared with others in damage mechanics [2], [16], and [27]. Few lacks are pointed out of the suggested method. Finally, an improvement of the static part of the characterization method is proposed and tested. This added part includes the used of the photogrammetry system ARAMIS to monitor the experimental tests and simulation of those tests with LS-Dyna.

Résumé

La présente maîtrise est réalisée à la demande de Recherche et Développement pour la Défense Canada (RDDC) à Valcartier. Dans un contexte militaire, la capacité à caractériser indépendamment un matériau pour la simulation numérique est primordiale for trois raisons. Premièrement, les matériaux utilisés ne sont pas répandus comme ceux utilisés en aéronautique ou bien en construction automobile. Deuxièmement, les paramètres des matériaux spécifiques au domaine militaire sont rarement divulgués. Troisièmement, l'utilisation d'alliages secrètement développés prohibe la caractérisation par une seconde entité. Le présent projet à pour objectif the permettre au RDDC Valcartier d'effectuer de faon indépendante la détermination des paramètres du modèle Johnson-Cook [1] [2] de matériaux ductiles. Pour arriver à ce point, le modèle Johnson-Cook est présenté à partir de la théorie de la mécanique de l'endommagement des milieux continus (CDM). La méthode de caractérisation proposée par Johnson et Cook dans les références [1] et [2] est introduite. Après quoi, les techniques et moyens expérimentaux nécessaires sont également décrits. Le reste du mémoire se concentre sur les paramètres statiques du modèle (A, B, n, D1, D2, et D3), puisqu'ils sont prédominants dans la modélisation de la mécanique de l'endommagement comparativement aux autres paramètres [2], [16], et [27]. Quelques lacunes sont observées dans la méthode proposée par les auteurs du modèle. Finalement, une amélioration est proposée pour la partie statique de la méthode de caractérisation. La technique utilisée pour cette proposition utilise le système photogrammétrique ARAMIS afin de mesurer les déformations locales des échantillons sur tout la plage de temps et de faciliter la corrélation avec les simulations numériques effectuées avec le code explicit Ls-Dyna.

Contents

List of Figures

List of Tables

Chapter 1

Introduction

Many engineering applications involve high strain rate deformations. Car crash, bird impact on aeronautic structures such as wing leading edge or engine intake, ballistic and high explosive military threats, and satellite protection against space debris are just few of the problems studied in the domain of high strain rates. Since experimental tests are very expensive, a lot of energy is put on material models and simulation methods that facilitate study of high strain rate problems.

The Johnson-Cook model [1], [2] is a visco-plastic model for ductile metals that consider strain rate effects on material behavior and fracture. This model is widely used since its first publication in 1983. Its parameters can be easily found in open literature for many materials [3].

1.0.1 Aim and motivations

In spite of parameters availability for many materials used in the aeronautics and in the automobile industry, in the context of the defence research, not a lot of publications give their material's parameters. They give rather general parameters taken from open literature. For this reason, it is of great importance for a research group as the Weapon Effects section of DRDC Valcartier to be autonomous in the characterization of materials for simulation and solving high strain rate deformation problems. The complete control of material characterization is even more important when secretly developped alloy are tested and modeled.

In the following chapters, we first present the theory behind the Johnson-Cook behavior and damage models. Then the Johnson-Cook parameters determination method is explained and discussed. Improvements to the quasi-static parameters determination is also suggested and tested in the present study.

Chapter 2

Continuum Damage Mechanics (CDM) of ductile metals

2.1 Introduction

Damage is the reduction in any way of one or more desired material characteristics. Here, damage is assumed to be caused by the creation of free surfaces of discontinuities. Damage affects material properties as follows:

- The elastic modulus decreases
- The yield stress before or after hardening decreases
- The hardness decreases
- The creep strain rate *increases*
- The ultrasonic waves velocity decreases
- The density decreases
- The electric resistance *increases*

Some of these property variations are used to evaluate qualitatively or quantitatively the damage evolution.

Damage mechanics represents the microstructural deformation and the failure process in terms of continuum parameters averaged over a small volume of material. Damage can be simply viewed as the intermediate process between a virgin material and macroscopic crack initiation.

It is important to understand that the material under analysis can be studied at three different levels:

- Microscale: Analysis of the accumulation of microstresses in the neighborhood of defects or interfaces and the breaking of bonds.
- Mesoscale: Analysis of the growth and coalescence of microvoids that will give origin to a crack.
- Macroscale: Analysis of the growth of the crack initiated at the mesoscale level.

The first two levels may be studied by damage variables of CDM (Lemaître, [5]). The third stage is usually studied using fracture mechanics. The following development of the theory about CDM is mainly based on the approach developped in Lemaître's book [5].

2.2 Damage growth

Bonds between atoms hold materials together. When debonding occurs, the damage process starts. The elastic moduli decreases with the increase of damage. Normally the constitutive equations of a material are written at a mesoscale level, incorporating properties of linearity and isotropy, which reflect atomic bonds deterioration process.

Because plasticity corresponds to crystal slip, there is no fundamental coupling between plasticity and damage. In metals, slips occur primarily by movements of dislocations. Dislocation may move by the displacement of bonds, thus creating a plastic strain by splip only, i.e., without any debonding. Any apparent coupling between damage and plasticity is due to a damage-induced increase of the effective stress.

At low levels of stresses in elastic-viscoplastic materials, the Cauchy stress tensor σ_{ij} is dependent only of the state of strain. Depending on the strain rate and above certain levels of stress, the yield stress changes with increasing plastic deformation and with the rate of this same deformation. Assuming for example a 1-D tensile test, the phenomena of elasticity, plasticity and viscoplasticity are represented in Figure 2.1.

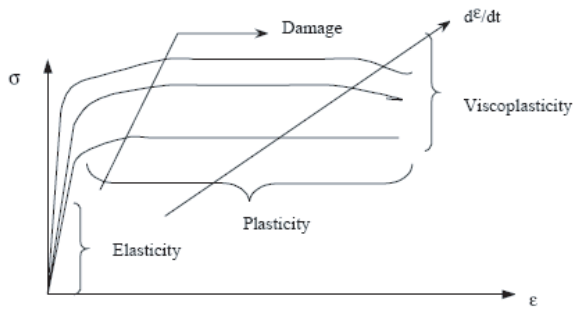

Figure 2.1: Representation of elasticity, plasticity and viscoplasticity phenomena for 1D tensile tests at different strain rates

The type of damage of interest here is known as *Ductile Plastic Damage*. This type is of particular interest for the dynamic applications. It involves the nucleation of cavities due to debonding, followed by their growth and coalescence ensuing from plastic instability in the slim links between damages zones. Figure 2.2 depicts damage, and its effect on plastic instability (negative stiffness).

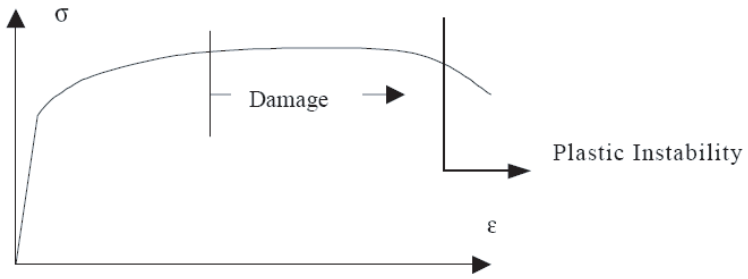

Figure 2.2: Representation of ductile damage and plastic instability

Isotropic damage can be defined as a scalar, $D_{(\vec{n})}$. This parameter can take any value between 0 and 1 and it satisfies:

- $D = 0$, represents an undamaged state
- $D = 1$, implies rupture of the element
- $0 < D < 1$, measures the current damage state

The damage variable is defined by the density of microcracks and microvoids, δS_D, lying on a plane cutting the reference volume element (RVE) of cross section δS.

$$D = \frac{\delta S_D}{\delta S} \tag{2.1}$$

The surface density of damage can be presented as

$$\delta S_D = \delta S - \delta \tilde{S}$$

then equation 2.1 becomes:

$$D = 1 - \tfrac{\delta \tilde{S}}{\delta S}.$$

where $\delta \tilde{S}$ is a conceptual surface that is still resisting to the stress.

In the next section, the formal description of elasto-(visco)-plasticity coupled with damage is presented.

2.3 Thermodynamics of damage

The thermodynamics of irreversible processes allows the modeling of different material's behavior in three steps:

1. Definition of state variables, the actual value of each parameter defining the present state of the corresponding involved physical deformation mechanism;
2. Definition of a state potential from which derive the state laws such as thermo-elasto-plastic stress and the definition of the variables associated with the internal state variables
3. Definition of a dissipation potential from which derive the laws of evolution of the internal state variables associated with the dissipative mechanisms

Note that the two potential functions introduce parameters which depend on the material and the temperature. They must be identified from experiments in each case (characterization tests).

These three steps offer several choices for the definitions, each chosen in accordance with experimental results and usage purpose. Then, the second principle of thermodynamics must be checked for any evolution.

2.3.1 General framework

The state variables, observable and internal variables, are chosen in accordance with the most important physical mechanisms of deformation and degradation of the material.

Table 2.1: State and associated variables (J. Lemaître [4])

Mechanisms	Type	State variables		Associated
		Observable	Internal	variables
Thermoelasticity	Tensor	ϵ_{ij}		σ_{ij}
Entropy	Scalar	T		s
Plasticity	Tensor		ϵ^p_{ij}	$-\sigma_{ij}$
Isotropic hardening	Scalar		r	R
Kinematic hardening	Tensor		α_{ij}	X_{ij}
Damage	Scalar (isotropic)		D	$-Y$
	Tensor (anisotropic)		D_{ij}	$-Y_{ij}$

The Helmholtz specific free energy taken as the state potential of the material is a function of all state variables. Written as $\psi(\epsilon^e_{ij}, Dor D_{ij}, r,\ \alpha_{ij},\ T)$, some qualitative experimental results on the possibility of couplings show that the state potential can be considered as the sum of thermo-elastic (ψ_e), plastic (ψ_p), and purely thermal

(ψ_T)contributions. Here, it is more convenient to consider the potential as the Gibbs specific free enthalpy ($\psi^\star$) deduced from the Helmoltz free energy by a partial transformation on the strain:

$$\psi^\star = \psi_e^\star + \frac{1}{\rho}\sigma_{ij}\epsilon_{ij}^p - \psi_p - \psi_T, \tag{2.2}$$

where ρ is the density and where ψ_p and ψ_T do not depend on the total strain. Now that the state potential is presented, the state laws can be derived from it. Following standard continuum mechanic practice, the usual laws of thermodynamics can be deduced.

Laws of thermoelasticity

- Strain decomposition
  $\epsilon_{ij} = \rho\dfrac{\delta\psi_e^\star}{\delta\sigma_{ij}} + \epsilon_{ij}^p \longleftrightarrow \epsilon_{ij}^e = \rho\dfrac{\delta\psi_e^\star}{\delta\sigma_{ij}}$
- Entropy
  $s = \dfrac{\delta\psi^\star}{\delta T}$

Other derivatives defining the associated variables

- Isotropic hardening
  $R = -\rho\dfrac{\delta\psi^\star}{\delta r}$,
- Kinematic hardening
  $X_{ij} = -\rho\dfrac{\delta\psi^\star}{\delta\alpha_{ij}}$,
- Damage
  $-Y = -\rho\dfrac{\delta\psi^\star}{\delta D}$ or $-Y_{ij} = -\rho\dfrac{\delta\psi^\star}{\delta D_{ij}}$

The **second principle of thermodynamics**, written as the Clausius-Duhem inequality is satisfied when damage rate, $\dot{D}$, is positive:

$$\sigma_{ij}\dot{\epsilon_{ij}^p} - \dot{w}_s + Y_{ij}\dot{D_{ij}} - \frac{q_i T_{,i}}{T} \geq 0 \tag{2.3}$$

This means that the mechanical dissipation is transformed into heat. Hence the reduced dissipation sum is composed of the dissipation due to plastic power ($\sigma_{ij}\dot{\epsilon_{ij}^p}$), minus the stored energy density rate ($\dot{w}_s = R\dot{r} + X_{ij}\dot{\alpha_{ij}}$), plus the dissipation due to damage ($Y_{ij}\dot{D_{ij}}$), and plus the thermal energy (q_i is the thermal flux).

All internal variables used here are governed by the kinetic laws that are derived from

a dissipation potential (F), which is assumed to be a convex function of the associated variables to ensure fulfillment of the second principle:

$$F = F(\sigma, R, X_{ij}, Y or Y_{ij}; Dor D_{ij}, T). \tag{2.4}$$

Introducing the plastic yield criterion or loading function (f), the nonlinear kinematic hardening term (F_X) and the damage potential (F_D), then according to qualitative experiments on the possibilities of coupling them, F can be decomposed additively as

$$F = f + F_X + F_D. \tag{2.5}$$

The constitutive equations and evolution laws can be formally written as

- Total strain decomposition
  $\epsilon_{ij}^T = \epsilon_{ij}^e + \epsilon_{ij}^p$,
- Elastic strain
  $\epsilon_{ij}^e = \frac{1+\nu}{E}\frac{\sigma_{ij}}{1-D} - \frac{\nu}{E}\frac{\sigma_{kk}}{1-D}$,
- Plastic strain rate
  $\dot{\epsilon_{ij}^p} = \dot{\lambda}\frac{\delta F}{\delta \sigma_{ij}}$,
- Isotropic hardening rate
  $\dot{r} = -\dot{\lambda}\frac{\delta F}{\delta R} = \dot{p}$
- Kinematic hardening rate
  $\dot{\alpha_{ij}} = -\dot{\lambda}\frac{\delta F}{\delta X_{ij}}$
- Kinetic law of damage evolution
  $\dot{D_{ij}} = \dot{\lambda}\frac{\delta F}{\delta Y_{ij}} = \alpha \cdot \frac{(D_{cr} - D_0)^{1/\alpha}}{\ln(\epsilon_f/\epsilon_{th})} \cdot R_\nu \cdot (D_{cr} - D)^{(\alpha-1)/\alpha} \cdot \frac{\dot{p}}{p}$.

The accumulated plastic strain rate ($\dot{p}$) is defined in accordance with the considered yield criterion . For the von Mises criterion this is given by

$$\dot{p} = \sqrt{\frac{2}{3}\dot{\epsilon_{ij}^p}\dot{\epsilon_{ij}^p}}. \tag{2.6}$$

In 1D (uniaxial tension-compression case), it simply means that $\dot{p} = |\dot{\epsilon_p}|$. The energy density release rate (Y), which is the variable associated with the damage variable, may be written as

$$Y = \frac{\tilde{\sigma}_{eq}^2 R_\nu}{2E}, \tag{2.7}$$

in which the triaxiality function is defined as

$$R_\nu = \frac{2}{3}(1+\nu) + 3(1-2\nu)(\frac{\sigma_H}{\sigma_{eq}})^2 \tag{2.8}$$

where σ_H is the hydrostatic stress, $\sigma_{eq} = \sqrt{\frac{2}{3}\sigma_{ij}^D \sigma_{ij}^D}$ the von Mises equivalent stress, and $\sigma_{ij}^D = \sigma_{ij} - \sigma_H \delta_{ij}$ the stress deviator. The ratio σ_H/σ_{eq} is the stress triaxiality denoted by σ^*.

2.4 CDM models

The whole set of constitutive equations is derived from the dissipation potential as explained in the general thermodynamics framework of Sect. 2.3.1. Here, few models are presented briefly. They differ by the choice of the analytic forms of the functions f, F_X, and F_D in the dissipation potential (eq. 2.5).

The elastic model is defined for $f < 0$, and the different plastic models are defined by

- Plasticity
  $f = 0, \dot{f} = 0,$
- Visco-Plasticity
  $f = \sigma_v > 0,$
- Isotropic Hardening
  $f = \sigma_{eq} - R - \sigma_y.$

The term σ_v is the viscous stress given by the law of viscosity. Mostly for viscous stress, the Norton power law and the exponential law are used (see, Lemaître [5]). The isotropic hardening use the von Mises criterion, where the σ_{eq} is the von Mises equivalent stress. The isotropic hardening R is related to the density of dislocation or flow arrests and it represents the growth in size of the yield surface.

The kinematic hardening governed by the back stress X is related to the state of internal microstress concentration. It represents the translation of the yield surface as X defines the center of the current elastic domain in the stress space. Nonlinear kinematic hardening is modeled by the potential function F_X,

$$F_X = \frac{3\gamma}{4C} X_{ij} X_{ij}, \tag{2.9}$$

with C and γ being temperature-dependent material parameters. A strong effect of the temperature (T) is observed as there is a transition from visco-plastic time-dependent (viscous) behavior at high temperature such as creep, to plastic time-dependent behavior at lower temperature.

2.4.1 Void growth based models

As this document is oriented toward high pressure and high strain rate application, it is important to present the void growth theory. The first model based on void growth

in ductile fracture have been proposed by McClintock [6], Rice and Tracey [7]. Both their models assume incompressibility grounded by experiments of Bridgman [8]. Those models attributes damage growth mainly to the triaxial state of stress. The following presents the McClintock's model and a generalized version of it from Hancock and Mackenzie [10].

McClintock proposed a cylindrical void with an elliptical cross section, under plane strain conditions. Such an element is presented in 2D in Fig. 2.3. Fracture is assumed to initiate when void reaches the boundaries of the element.

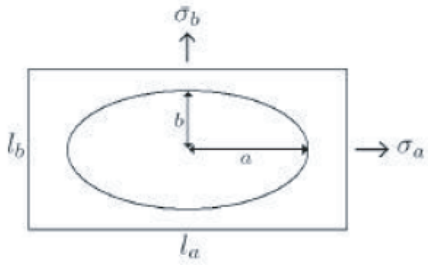

Figure 2.3: Void element proposed by McClintock

Where l_a, l_b are the element's lengths and a, b are the corresponding semi-axes lengths of the hole. In a first step, McClintock introduced two hole-growth factors for each direction a and b: $F_a = (a/l_a)/(a_0/l_a^0)$ and $F_b = (b/l_b)/(b_0/l_b^0)$. Fracture occurs when no cross-section area is left at least in one direction, i.e. when $a = \frac{1}{2}l_a$ and/or $b = \frac{1}{2}l_b$. Then the failure criteria are written as

$$F_a = F_a^f = \frac{1}{2}(l_a^0/a_0) \tag{2.10}$$

$$F_b = F_b^f = \frac{1}{2}(l_b^0/b_0) \tag{2.11}$$

McClintock suggested an additive damage parameter that accumulates to unity at fracture. This damage parameter as introduced in Sect. 2.3.1 is written as

$$\delta D_{a,b} = \delta \ln(F_{a,b})/(F_{a,b}^f). \tag{2.12}$$

From the equilibrium equation $\nabla \cdot \sigma = 0$, McClintock derived a fracture strain assuming incompressible and plane strain. He formulates the strain to fracture as

$$\tilde{\epsilon}^f = \frac{2}{\sqrt{3}} \ln(\frac{l_b^0}{2b_0}) \exp(-\frac{\sqrt{3}}{2}\frac{\sigma_a + \sigma_b}{\bar{\sigma}}) \tag{2.13}$$

Hancock and Mackenzie [10] demonstrated that void coalescence has no prefered direction. Therefore an average growth factor stands by itself. They showed that the average

growth factor, $(F_a F_b)^{\frac{1}{2}}$, for all the notches and for both specimens of their experiments were similar. Then it seems more appropriate to take the triaxial ratio, $\sigma^* = \frac{\sigma_m}{\bar{\sigma}}$, as the parameter to define the state of stress rather than $\frac{\sigma_a + \sigma_b}{\bar{\sigma}}$, [10]. Rice and Tracey [7] confirmed this assumption that fracture by coalescence of voids is accelerated by a high-level of triaxiality.

Hancock and Mackenzie generalized the equations 2.12 and 2.13 with three material parameters:

$$\epsilon^f = D_1 + D_2 \exp\left(D_3 \frac{\sigma_H}{\sigma}_{eq}\right), \tag{2.14}$$

where D_1 is taken as the void nucleation strain.

Chapter 3

Johnson-Cook model

Johnson and Cook [2] have extended the damage model of Hancock and Mackenzie presented in chapter 2, eq. 2.14. They extended this strictly triaxial ratio dependent model so as to consider high strain rate and high temperature effects on the strain to fracture of ductile metals.

Because plasticity and damage are impossible to distinguish during a tensile test for example, the Johnson-Cook behavior model [1] must first be presented.

3.1 Johnson-Cook behavior model

Lemaître [5] presents the CDM models that represent the equivalent stress as

$$(\sigma - X)_{eq} = \sigma_y + R + \sigma_v. \tag{3.1}$$

The kinematic and the isotropic hardening parameters, X and R respectively, the yield function, σ_y, and the viscous stress, σ_v, decompose the equivalent stress. The problem is that those phenomena are very hard to differentiate during the plasticity regime of a material.

Johnson and Cook [1] consider no kinematic hardening and express rather the equivalent stress as a function of plastic strain, strain rate and temperature. Those variables are easier to measure and hence their associated parameters. The Johnson-Cook model is an empirical relationship for the flow stress, σ_{flow}, which is represented as

$$\sigma_{flow} = [A + B\epsilon^n][1 + C \ln \dot{\epsilon}^*][1 - (T^*)^m], \tag{3.2}$$

where A, B, C, n and m are the material constants, ϵ is the plastic strain, $\dot{\epsilon}^* = \dot{\epsilon}/\dot{\epsilon}_0$ is the dimensionless plastic strain rate for $\dot{\epsilon}_0 = 1s^{-1}$, and the non dimensional temperature T^* is defined as

$$T^* = \frac{T - T_{room}}{T_{melt} - T_{room}}. \tag{3.3}$$

The determination of the five material constants is described further in this chapter. The first set of brackets of equation 3.2 represents the stress as a function of strain

for $\epsilon_0 = 1s^{-1}$ and $T^* = 0$. Others represent the dynamic and the temperature effect on stress flow, respectively. When adiabatic conditions occur (i.e. on high strain rate loading) all internal plastic work is assumed to be converted into heat (temperature increase):

$$\Delta T = \frac{\bar{\sigma}\bar{\epsilon}^p}{\rho C_\nu}, \tag{3.4}$$

where $\bar{\sigma}$ is the effective stress, $\bar{\epsilon}^p$ is the effective plastic strain, ρ is the mass density and C_ν is the constant volume specific heat.

3.1.1 Behavior model's constants determination

The method presented here is simple and consider that cross effects between the strain, strain rate and the temperature on the stress flow are well caught by the product of the three brackets. Thus we can process different tests that isolate static, dynamic and thermal parameters from other brackets. This is one of the reasons why the Johnson-Cook model is easy to use.

The determination of the behavior model's constant is well described by Holmquist and Johnson [13]. The main idea is to isolate each parameter by gathering data in specific conditions and by manipulating those data in the right graphics. Three curves of the equivalent flow stress versus the equivalent plastic strain must be built: one on quasi-static and isothermal conditions, two at strain rates (adiabatic conditions at high strain rate) related to the simulated phenomenon. For reasons explained in Sect. 3.1.2 temperature term should only be used to model high temperature effects at high strain rates. If the temperature term is wanted, at least another curve at high temperature must be generated at one of the high strain rate explored previously. Curves come from tensile, torsion, or compression tests. Generally tensile and torsion tests data are affected by the Bridgman and the von Mises factor, respectively, to balanc! e effects of the evolution of the state of stress in the characterization specimens. Those factors are treated in Sect. 4.1.1, and 4.1.3. In Sect. 4.1.1 some warnings are presented about the use of the Bridgman factor for tensile test data.

The parameter A corresponds to the yield stress of the quasi-static curve. To obtain the parameters B and n, some manipulations are done on the data of the quasi-static curve:

1. Data corresponding to the elastic behavior ($\epsilon < \epsilon_{yield}$) are taken away to keep only the plastic part of the curve.

2. Then plastic data, $\sigma - \sigma_{yield}$ versus $\epsilon_{plastic}$, are drawn in a $\log - \log$ graph. The B parameter is then the value of $\sigma - \sigma_{yield}$ at $\epsilon_{plastic} = 1$. While n is the slope of the curve drawn in the $\log - \log$ graph.

The strain rate parameter, C, is determined from the three curves at room temperature, T_{room}. A curve of the flow stress versus the logarithm of the strain rate is drawn from one datum point of each flow stress-strain curve. Those datum points represent the flow stress at different strain rate, but at the same plastic strain and at room temperature. C is then the slope of this curve.
The thermal parameter, m, is deduced by a simple calculus developed as:

$$m = \frac{\log(1 - \frac{\sigma}{\sigma_{room}})}{\log T^*} \tag{3.5}$$

where σ_{room} is the stress for a determined plastic strain and strain rate at room temperature, T^* is the normalized temperature of eq. 3.3 and σ is the stress for the same plastic strain at high temperature (from the last curve mentioned).

Tensile, compression, or torsion tests can be performed to gather necessary curves. The best would be to use characterization tests that are as close as possible to the phenomena to be simulated in a state of stress point of view. The problem is however the same with all characterization tests; the closer to complex phenomena a test is, the harder it is to isolate parameters from it. In many situations, money and time are the most restrictive factors. Often the rule "simplest is the best" applies.

3.1.2 Behavior model criticism

A good model has to represent phenomena (here a material behavior) with the best accuracy without being too complex. With complexity come difficulties to get model's parameters from material characterization tests.

Stress-strain behavior

The model can accurately represent the yield and the plastic flow. However, its use should be limited for isotropic material modeling.

Stress-strain rate behavior

With the evolution of the knowledge of metals behavior, T.J. Holmquist and G.R. Johnson [13] report evidence that the strain rate effect on material strength is not a linear function of the natural log (as the herein presented version indicates), but rather an exponential function of the natural log. In fact, the strengthening with the strain rate accelerates rapidly at high strain rates for many metals [15]. This is due to a change in deformation rate's mechanism. At lower strain rates, the deformation rate is controlled by the cutting or by-passing of discrete obstacles by dislocations. At higher rates, the deformation rate is controlled by phonon or electron drag on moving dislocations. Unfortunately, the Johnson-Cook behavior model does not consider the second mechanism, which can lead to softer predictions compared to reality when modeling

high strain rate phenomenon with such metals.

W.R. Rule and S.E. Jones [14] proposed and implemented a revised form for the Johnson-Cook strength model in EPIC. This revised model aims for a better strain rate sensitivity at very high strain rates ($> 10^3\ s^{-1}$) without compromising the good accuracy of the original model eq. 3.2 at low and moderate strain rates. Rule and Jones also give a simple numerical procedure to determine the three added parameters.

Stress-temperature behavior

Lesuer [16] observed strain rate dependency of the temperature term. At high temperature the model represents well the stress-temperature response. At low strain rates, the model predicts stresses that are significantly higher than stresses observed experimentally. Therefore, the Johnson-Cook model represents well stress-temperature effects occurring at high strain rates and so should be used to model room temperature structure heated by high strain rate hardening.

3.2 Equation of state

Hydrodynamic material models such as the Johnson-Cook require an equation of state (EOS) when used with solid elements, since hydrodynamic models only compute the deviatoric stresses. EOS is also needed for the Johnson-Cook damage when using the tensile failure criterion of dynamic spall or pressure cutoff (see Sect. 3.3.1). An EOS defines the pressure-volume relationship. LS-Dyna [17] allows to use two different EOS with the Johnson-Cook behavior model: the Linear Polynomial and the Grüneisen.

3.2.1 Polynomial EOS

For low strain rate process, the linear polynomial EOS is normally used. The pressure calculated by this EOS is given by

$$p = C_0 + C_1\mu + C_2\bar{\mu}^2 + C_3\mu^3 + (C_4 + C_5\mu + C_6\bar{\mu}^2)E \tag{3.6}$$

where the excess expression μ is given by

$$\mu = \frac{\rho_0}{\rho} - 1 \tag{3.7}$$

where ρ is the current density, ρ_0 is the initial density, C_i are constants, and E is the internal energy [18]. The tension-limited excess compression is expressed as

$$\bar{mu} = max(\mu, 0) \tag{3.8}$$

which is the maximum positive excess compression value. The linear polynomial EOS is linear in internal energy, and may be used to fit experimental data for many materials.

3.2.2 Grüneisen EOS

The Grüneisen EOS may be the best choice for high velocity impact regime as well as high speed structure dynamics [19]. The Grüneisen EOS is given by

$$p = \frac{\rho_0 C^2 \mu \left[1 + \left(1 - \frac{\gamma_0}{2}\right)\mu - \frac{a}{2}\mu^2\right]}{\left[1 - (S_1 - 1)\mu - S_2\frac{\mu^2}{\mu+1} - S_3\frac{\mu^3}{(\mu+1)^2}\right]^2} + (\gamma_0 + a\mu)E \tag{3.9}$$

and for expanded materials as

$$p = \rho_0 C^2 \mu + (\gamma_0 + a\mu)E \tag{3.10}$$

where C is the sound speed in the material, S_1, S_2, and S_3 the coefficients of the slope of the shock speed versus the particle speed curve, $U_s - U_p$; γ_0 is the Grüneisen gamma; a is the first order volume correction to γ_0; and μ is the same parameter as in the linear polynomial EOS. The Grüneisen gamma and μ are given respectively by

$$\gamma_0 = V\left(\frac{\partial P}{\partial E}\right)_V, \tag{3.11}$$

$$\mu = \frac{\rho}{\rho_0} - 1. \tag{3.12}$$

Note that parameters C, S_1, S_2, and S_3 are simply the constants of the third order polynomial approximation of the curve $U_s - U_p$.

$$U_s = C + S_1 U_p + S_2 U_p^2 + S_3 U_p^2 \tag{3.13}$$

Often, this curve can be accurately approximated by a linear approximation, which reduce most of the time S_2 and S_3 to zero. All those parameters are easily found in literature [11].

3.3 Johnson-Cook damage model

The Johnson-Cook damage model [2] is a cumulative-damage fracture model that takes into account the loading history, which is represented by the strain to fracture. The strain to fracture is expressed as a function of the strain rate, temperature, and pressure. Hancock and Mackenzie [10], and Hancock and Brown [20] tell that the strain to fracture is mostly dependent of the stress state. In other words, parameters D_1, D_2, and D_3 are predominant compared with the two others, and therefore should be found out carefully. J-C is an instantaneous failure model, which means that no strength or stiffness remains

after erosion (failure) of an element, at least in tension. Different possible after-rupture stiffness modes are available with the LS-Dyna software, and will be presented further in this section. The damage to an element is defined by

$$D = \sum \frac{\Delta\epsilon}{\epsilon^f} \tag{3.14}$$

where $\Delta\epsilon$ is the increment of the equivalent plastic strain which occurs during an integration cycle, and ϵ^f is the equivalent strain to fracture under the current conditions of pressure and equivalent stress, strain rate, and temperature. The fracture of an element is allowed when $D \geq 1.0$ for this element. The general expression for strain at fracture is given by

$$\epsilon^f = [D_1 + D_2 \exp D_3\sigma^*][1 + D_4 \ln \dot{\epsilon}^*][1 + D_5 T^*] \tag{3.15}$$

for constant values of the variables (σ^*, $\dot{\epsilon}^*$, and T^*) and for $\sigma^* \leq 1.5$. The dimensionless pressure/stress ratio (mentioned as σ^* in Sect. 2.3.1) is a measure of triaxiality of the stress state and is defined as

$$\sigma^* = \frac{\sigma_H}{\sigma_{eq}} \tag{3.16}$$

The dimensionless strain rate $\dot{\epsilon}^*$ is equal to $\dot{\epsilon}/\dot{\epsilon}_0$, where $\dot{\epsilon}_0$ is a unity strain rate. T^* is the homologous temperature defined by eq. 3.3. Figure 3.1 gives the failure criterion at triaxial ratio larger than 1.5.

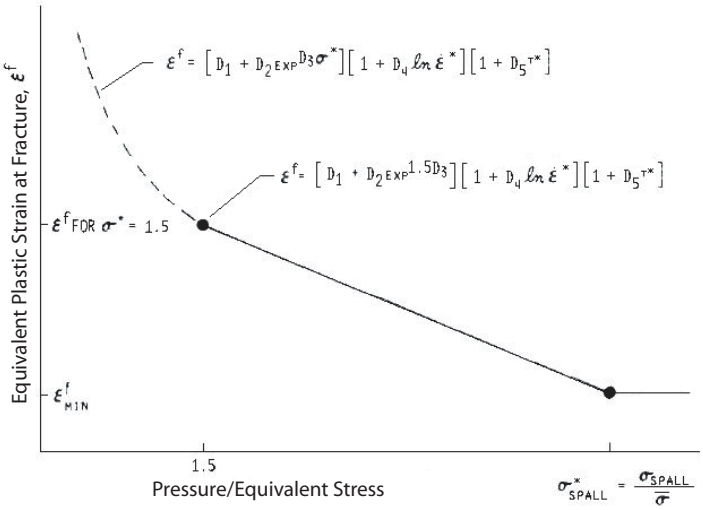

Figure 3.1: Strain to fracture criterion at high triaxial ratio, $\sigma^* > 1.5$

3.3.1 Spall models

LS-Dyna [17] proposes a choice of three spall models with the use of the Johnson-Cook model with the brick element. A spall model is used to represent material damaging under tensile loads. The limiting pressure model limits the minimum hydrostatic pressure to the specified value, $p \geq p_{min}$. If the pressure calculated in an element is more tensile then this limit, the pressure in this element is reset to p_{min}. The deviatoric stresses are still active and so this model is not strictly a spalling model. Note that the tensile cutoff is constant throughout the analysis. The hydrostatic tensile spall model is similar to the preceding model, except that when p_{min} is reached, the deviatoric stress is reset to zero for the rest of the analysis, and only compressive hydrostatic pressure is considered, otherwise the hydrostatic tension is reset to zero. The maximum principal stress spall model reset to zero the deviatoric stress and allow no hydrostatic tension when the maximum principal stress, σ_{max}, exceeds the limit value σ_p.

3.3.2 Damage model's constants determination

Many authors use the Johnson-Cook damage model in their simulation, but only a few gather their own damage parameters. Johnson and al. [2], [12] describe without many details the technique used to get the parameters widely employed by users of this model. Kay [21] presents a complete description of the characterization tests performed to get the damage parameters. Its method seems slightly different from the one described by Johnson and al., since he characterizes the material used only at high strain rate and deduce the pressure and temperature parameters. Wierzbicky and al. [22], and Bao and Wierzbicky [23] concentrate their efforts on the development of characterization tests from negative to high positive triaxiality, and so as to get the first three damage parameters, which are the most important of the model. Here a tentative is made to describe the process used to obtain all damage parameters.

To determine the damage model's constants, the strain to failure is to be established in function of the triaxial state of stresses. This step gives the constants D_1, D_2, and D_3. After that, strain rate parameter, D_4, and temperature parameter, D_5, can be found. All parameters needs characterization tests, and some numerical simulations to be performed. Both characterization tests and numerical simulations are exhaustively described in Chapter 4 and Chapter 6, respectively. The following is a step by step method to obtain each parameters.

Triaxial stress state (D_1, D_2, and D_3)

At least, three tests must be made to build the exponential curve of the strain to fracture in function of the stress triaxiality, σ^*, and find the corresponding equation. In this study, for logistical reasons, the triaxiality characterization tests are made on isothermal and quasi-static conditions. There is no need to do those tests at high strain

rate, since cross effect with strain rate parameter is taken into account when the first two brackets are multiplied.

The three tests are axisymmetric tensile tests. To find three different stresses triaxiality at failure, specimens are of different form. Specimens have the same minimum cross section's diameter, which here is 8mm. The first is unnotched, the second and the third have a 4mm and a 6mm notch's radius, respectively.

The state of stress that prevails inside the specimen at its failure is impossible to measure directly during the experiment. It is also hard to calculate it analytically from experimental measurements in uniaxial tensile test on axi-symmetrical specimens. Even more, the triaxial state of stress changes during the loading process due to renotching.

The strategy employed in this project to get the first three parameters, is to model the characterization tests and to fine tune the parameters till the strain to rupture match the experimental measurements (strain on few key locations on the specimen and diameter at notch center). To build the curve, the triaxial ratio chosen is the one followed by the specimen gage just before the almost instantaneous fracture of the specimen. To get this information, each tests should be at least filmed. Section 5.1.3 presents an imaging system that can compute with a good precision the displacement and the deformation of a specimen with more or less preparation.

After the triaxial states of stress are obtained for each specimen, a best curve fit should be drawn in strain to failure versus triaxial ratio graph. By a least square regression, the parameters that give the best fit curve are then found.

High strain rate stress state (D_4)

For parameter D_4, only torsion tests at different shear strain rates need to be performed. Tensile tests could be done either with a tensile split Hopkinson tensile bar apparatus, however since it is much more complex, the Kolsky torsion bar is preferred. Moreover, torsion tests prevent pressure effects to interfere on the strain at failure under high strain rate deformations.

Tests should cover the high strain rate regime that is explored during the simulated phenomenon . Then few data points of shear strain to fracture at different strain rates are converted into equivalent strain to fracture with the von Mises factors, eq. 4.17. With the equivalent strain at fracture data collected from quasi-static tests, a curve of the strain at fracture versus the strain rate can be drawn from quasi-static to high strain rates. Those dynamic tests are performed with a Kolsky torsional bars apparatus. An detailed description of the apparatus is done in the experimental chapter 4.

To obtain parameter D_4, a curve of a "reduced" strain to failure $((\epsilon_f - (D_1 + D_2))/(D_1 + D_2))$versus the strain rate should be drawn in natural semi-log graph. D_4 is then the slope of the curve obtained. Note that this curve should be built from tests carried out at room temperature.

High temperature environment (D_5)

We get the D_5 parameter by the same technique used for the parameter D_4 and at high strain rate. This time, the shear strain to failure versus the shear strain rate curve must be generated at different temperatures. This experiment should be done at temperatures that are close to those encountered in the problem to be modeled.

The temperature parameter, D_5, is found by drawing a "reduced" strain to failure $((\epsilon_f - (D_1 + D_2)(1 + D_4 \ln(\dot{\epsilon}^*)))/((D_1 + D_2)(1 + D_4 \ln(\dot{\epsilon}^*))$ versus temperature. All those data should be collected at high strain rate.

3.3.3 Damage model criticism

Damage evolution and strain to failure are mostly linked to triaxiality. For this reason, the following criticisms are voluntarily focusing on the first bracket of the damage model.

Triaxiality dependency of the strain to failure

By the observations made on spall phenomenon by Nicholas and Rajendran [24], the first bracket of the Johnson-Cook model seems to be valid. The non dimensional parameter σ^* has been introduced by Hancock and Mackenzie [10], and Hancock and Brown [20]. They recognized that strain to failure is not strictly a material constant but, rather, depends strongly on the state of stress. They demonstrated the effect of stress triaxiality on the strain to fracture through quasi-static experiments on notched tensile specimens. They showed that the fracture strain decreases with increasing hydrostatic pressure as shown in the high triaxiality part of Figure 3.2. This means that for a negative stress state (pressure), the strain to fracture is higher than in a case of a positive stress state (tension). This behavior explains why the parameter D_3 is always negative. In Figure 3.2, the mixed mode does not always show an increase of the plastic strain with an increase of the hydrostatic pressure. It depends on the difference between the value of the effective strain to failure at the end of the "Shear Fracture" zone ($\sigma^* = 0$) and at the beginning of the "Void Growth" zone ($\sigma^* \approx 0.4$).

Wierzbicki and al. [22, 23] have studied in details the dependency of the strain to fracture on the triaxial state of stress. Johnson and Holmquist [26] consider tensile tests with high triaxiality ratio to provide D_1, D_2 and D_3 parameters for many materials. They also performed torsion tests (triaxiality equals zero), but often consider them "insubordinate", and then excluded them from the curve fitting procedure. Instead, Wierzbicki and al. survey a larger range of triaxiality by mean of different experimental specimens to gather for example experimental points shown on Figure 3.2. Wierzbicki and Bao carried out, in [22], rupture tests on 2024-T351 aluminum to observe the range of small, even negative triaxial ratio effect on strain to rupture. They came with the

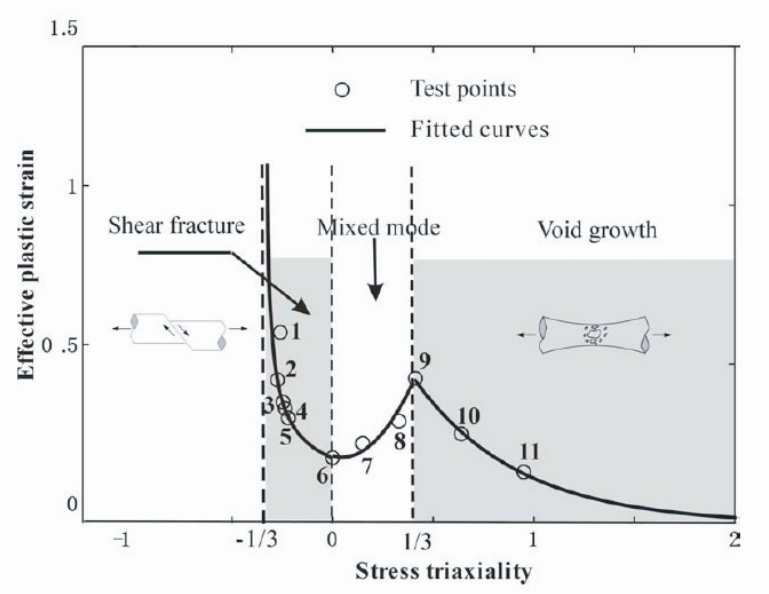

Figure 3.2: Variation of the effective plastic strain at failure with triaxiality of the state of stress for 2024 T351 Aluminum, from [22].

graphs shown in Figure 3.2, where we can see that the first bracket of the Johnson-Cook da! mage model considers well only the fracture due to void growth. In other words, the Johnson-Cook damage model considers only the fracture due to high triaxial state of stress. It does not take into account the failure caused by shear, and by ricochet often represent poorly the mixed mode. Therefore, it is understandable why the pure torsion data of Johnson and Holmquist seems to be insubordinate. Bao and Wierzbicki [23] even demonstrate the presence of a cut-off value of negative triaxiality for fracture of different metals under which no failure mode is possible. This cut-off is also visible on Figure 3.2 at $-1/3$ of stress triaxiality.

Wierzbicki and al. [22] present the Xue-Wierzbicki (X-W) fracture criterion. Teng and Wierzbicki [25] compared the X-W fracture criterion with the Johnson-Cook and a constant strain to failure criterion for high velocity perforation of a thin beam. In this study, materials carry strain rates up to $10^4 - 10^5\, s^{-1}$. Teng and Wierzbicki conclude that the Johnson-Cook model and constant strain to fracture model were found to induce large eroded area under the impacted surface, which is the high pressure zone. They compared many levels of fracture strain and concluded as well that the perforation process is not much sensitive to the magnitude of fracture strain, since the strain is very localized around the crack tip, and the strain level in this area exceeds easily the threshold value. On the other hand, they found that the perforation process was well sensitive to the cut-off value, which prevents element erosion under highly negative ! triaxi al ratio (high pressure) state of stress.

Strain rate and temperature dependency of the strain to fracture

Contrarily to the behavior model, the strain rate and the temperature effect on the strain to fracture level is much smaller for many materials. This remark has been done by many authors: Johnson and Holmquist [26] as quoted by Lesuer [16], Johnson and Cook [2], and Anderson and al. [27].

Chapter 4

Experimental methods

As mentioned in the previous chapters, the Johnson-Cook model asks specific characterization tests to determine its parameters. When using the Johnson-Cook model in numerical simulation software such as Abaqus and LS-Dyna, basic parameters as density, Poisson ratio and Young modulus must be provided. Those parameters can be easily found in the literature. Thus, the following will focus on experimental tests specifically needed to get Johnson-Cook parameters. Note that only few parameters like the Young modulus and the yield stress can be easily confirmed during the following tests.

In the frame of this present work, no high strain rate and high temperature experimental test results are use for many reasons. Nevertheless the following paragraphs are describing the high strain rate and temperature experimental techniques that will be use in a futur work.

4.1 Quasi-static

Since the Johnson-Cook model is based on quasi-static theory that has been upgraded by including strain rate and high temperature factors, quasi-static tests give most of their parameters. This section describes quasi-static tensile test on initially unnotched and notched specimens. It gives the definition of measurable parameters and how they lead to Johnson-Cook model's parameters.

4.1.1 Unnotched tensile test theory

Testing equipment

For low strain rate tensile test, two general types of machines are used: load controlled machines and displacement controlled machines. In the present study, the second group has been preferred, since it is stiffer than the load controlled ones and thus it reproduces more accurately the shape of the load-displacement curve. A stiffer machine reduces

also oscillation's amplitude of the strain rate caused by the machine's elongation. Here, an Instron 1137 screwdriven machine is used. Specimens are pulled at constant speed from one end by a movable crosshead, while the other is fixed.

From the crosshead velocity, v, the true strain rate before necking can be calculated as

$$\dot{\epsilon} = \frac{v}{L} \tag{4.1}$$

where L is the current specimen's length. Equation 4.1 indicates that for a constant crosshead speed the true strain rate will decrease as the specimen elongates. The true strain rate in the necked region can be calculated during the whole tensile test as

$$\dot{\epsilon} = -\frac{1}{A}\frac{dA}{dt} \tag{4.2}$$

Engineering stress-strain curve

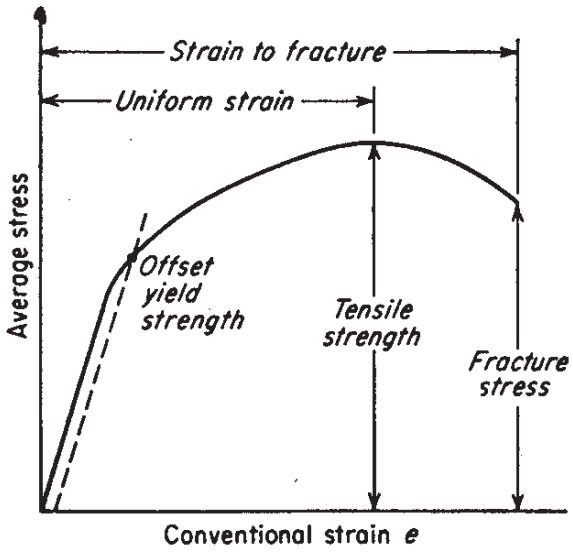

Figure 4.1: Engineering stress-strain curve showing the uniform strain part and the unstable part to the strain to fracture.

When using a displacement controlled machine, the basic outputs provided by it are: the loading, the displacement of the crosshead, and the elapsed time. Usually, engineering stress-strain curves (see Fig. 4.1) are deduced from loading and corresponding displacement with the initial geometry of the specimen and the following equations.

$$s = \frac{P}{A_0} \tag{4.3}$$

$$e = \frac{\delta}{L_0} \tag{4.4}$$

where P is the loading, δ is the elongation of the gage length, while A_0 and L_0 are the initial cross-section area and gage length of the cylindrical specimen, respectively.

Yielding

Often, the ultimate tensile strength (UTS), s_u, is used in design to evaluate the strength of a metal.

$$s_u = \frac{P_{max}}{A_0} \tag{4.5}$$

where P_{max} is the maximum load applied to the specimen. The UTS is of little fundamental significance with regards to the strength of a metal. As it is shown in figure 4.1 the metal part has already plastified when this value is reached. Engineers use safety factors to be sure that the part does stay in a safe range of strain.

The yield strength, s_0, is the stress required to produce a small specified amount of plastic deformation. This amount is usually specified as a strain of 0.2 or 0.1 percent. This stress gives a good idea of a material strength. Here, a strain of 0.2 percent is used ($e = 0.002$).

$$s_0 = \frac{P_{(e=0.002)}}{A_0} \tag{4.6}$$

Plastic deformation

The assumption of constant volume is usually valid in the uniform strain range illustrated in figure 4.1. For this range, it means that the cross-sectional area reduces uniformly along the specimen's gage proportionally to the elongation. Initially the strain hardening compensates more than for the decrease in area. Eventually, a defect in the specimen introduces stress concentration in a small volume of material. This leads to an instability called necking. All further plastic deformation is then concentrated in this region.

The beginning of the neck formation corresponds with the UTS, since after this point, on the engineering stress-strain curve, the decrease in specimen cross-sectional area is greater than the increase in deformation load arising from strain hardening.

Ductility

The conventional measurements of ductility that are obtained from the tension test are the engineering strain at fracture, e_f (usually called elongation), and the reduction of area at fracture, q. Both of these properties are obtained after fracture by putting the specimen back together and taking measurements of the length after at fracture, L_f, and the diameter at fracture, D_f. Hence the fraction of elongation due to elastic strain

is neglected.

$$e_f = \frac{L_f - L_0}{L_0} \tag{4.7}$$

$$q = \frac{A_0 - A_f}{A_0} \tag{4.8}$$

An appreciable fraction of the plastic deformation is concentrated in the necking zone of the tensile specimen, thus the value e_f depends on the gage length L_0 over which the measurement is taken. Therefore, when reporting values of percent elongation, the gage length L_0 should always be given.

True-stress-True-strain curve

Since the specimen does not conserve its original geometry, the engineering stress-strain curve does not give a true indication of the deformation characteristics of the metal tested. Figure 4.2 shows how true stress-true strain curve and its correction for necking is qualitatively different from the engineering stress-strain curve.

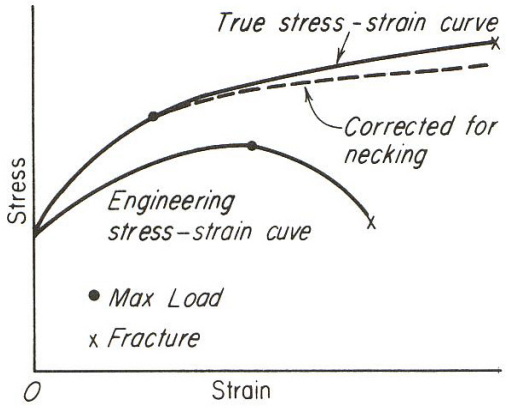

Figure 4.2: The true stress-true strain curve considers the cross sectional area change during the test, not the engineering curve, but still need to be corrected since the uniaxial state of stress is not anymore valid at the time necking begins.

The true stress and true strain are given as

$$\sigma = \frac{P}{A} \tag{4.9}$$

$$\epsilon = \ln \frac{L}{L_0} \tag{4.10}$$

where A is the current smallest cross-section area. In term of engineering stress and strain, the true stress can be calculated as

$$\sigma = \frac{P}{A_0}(e+1) = s(e+1) \tag{4.11}$$

Note that equation 4.11 assumes a constant volume and a homogeneous distribution of strain along the gage length. In other words, equations 4.9 and 4.11 are no more valid when necking begins.

Beyond the maximum load, the true strain should be based on the actual area or diameter measurements.

$$\epsilon = \ln\frac{A_0}{A} = 2\ln\frac{D_0}{D} \tag{4.12}$$

Note that the last part of equation considers circular cross-section of the neck, which could be not exact in the case of an inhomogeneous metal as rolled steel or aluminum plate.

Bridgman factor

When tensile tests are conducted up to a certain plastic strain, a complex triaxial stress arises in the plastified region. A notch under tension produces radial, σ_r, and transverse, σ_t, stresses (see Fig. 4.3). The hydrostatic tension decreases ductility. This has the effect of raising the value of the longitudinal stress mainly near the central axis. Therefore, the average true stress at the neck is higher than the stress required to cause flow when strictly axial tension was prevailing. That is why the stress-strain curve seems to fall while a hardening is expected (see Fig. 4.1). A complete study of large plastic flow and fracture is made by Bridgman himself in [8].

Bridgman [8] made a mathematical analysis that provides a correction to the average axial stress to compensate for the introduction of transverse stresses. This analysis was based on the following assumptions for cylindrical specimen (see Fig. 4.4):

1. An circular arch approximates the contour of the neck.
2. The cross section of the necked region remains circular throughout the test.
3. The von Mises yield criterion applies.
4. The strains are constant over the cross section of the neck.

According to this analysis, the uniaxial flow stress corresponding to the tension existing in a tensile test if necking had not introduced triaxial stresses is:

$$\sigma = \frac{(\sigma_x)_{avg}}{(1+\frac{2R}{a})[\log(1+\frac{a}{2R})]} \tag{4.13}$$

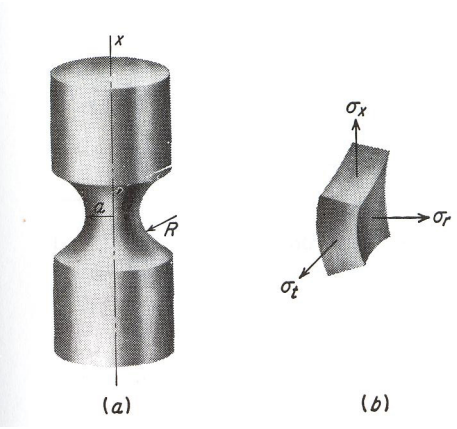

Figure 4.3: a)Necking or notch geometry variables and b) principal stresses of an uniaxial specimen.

where a is the cross section radius, R is the neck radius and $(\sigma_x)_{avg}$ is the measured stress in the axial direction:

$$(\sigma_x)_{avg} = \text{Load/Minimum cross section.}$$

The values of a/R ration can be obtained either by straining a specimen at a given amount beyond necking and unloading to measure a and R directly, or by measuring these parameters continuously past necking using photography or a tapered ring gage. Bridgman [8] presents also an experimental curve that gives a good approximation of this parameter. For better results, this curve can be built for a specific material.

The Bridgman method supported by the same previous hypothesis can also lead to the triaxial ratio anywhere on the cross section at neck's root. On this area, Bridgman's approach states that the triaxial ratio is only dependent on the geometry of the specimen at the neck.

$$\frac{\sigma_h}{\sigma_{eq}} = \frac{1}{3} + \ln(\frac{a^2 + 2aR - r^2}{2aR}), \tag{4.14}$$

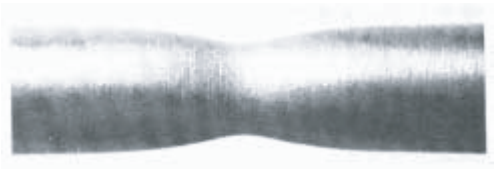

Figure 4.4: Cylindrical specimen necking under tension

Criticism of the Bridgman factor

Note that it is difficult to verify the veracity of the correction brought by the Bridgman factor, because true stresses after necking cannot be measured, fortunately assumptions that support it can be challenged. A criticism and a mathematical development of the Bridgman correction method are presented by Ling [30]. Many articles from different references evaluate the error brought by the use of the Bridgman factor to get the equivalent stress out of a True-Stress-True-Strain curve for the post-necking phase. They mainly question two assumptions made by Bridgman. La Rosa et al. [31] and [32] prove that the assumption of uniform flow stress distribution over all the neck section is wrong, and this is caused by a large deviation from uniformity of the strain distribution. Alves and Jones [33] obtained results that show that the state of stress at the notch root of a tensile specimen depends also on material properties and not only on the geometry as stated by Bridgman.

True fracture stress

The true fracture stress is the load at fracture divided by the cross-sectional area at fracture. This stress should be corrected for the triaxial state of stress existing in the tensile specimen at fracture (time and diametral location). Since data are required for this correction are often not available, true-fracture-stress values are frequently in error. The triaxial strain will be approximated by a numerical simulation of the tensile test with different axisymmetric shapes (see Chap. 6).

True fracture strain

The true fracture strain can be calculated as

$$\epsilon_f = \ln \frac{A_0}{A_f} \tag{4.15}$$

It can not be calculated from the measured value of e_f. However, for cylindrical tensile specimens the reduction of area q is related to true fracture strain by the following relation.

$$\epsilon_f = \ln(\frac{1}{1-q}) \tag{4.16}$$

Notched tensile test

Smooth axisymmetric specimens are tested in tension to obtain the quasi-static parameters of the behavior model . Since notch induces triaxial stress field, it reduces local ductility. In this study, notched specimens are tested in addition to smooth specimens with the aim of measuring the influence of the triaxial stress on the fracture strain of the metal.

4.1.2 Quasi-static tensile test method retained

From the previous discussion, the Bridgman method will not be used in the present study. For the strength model characterization, it would mean that only the pre-necking part of the True-Stress-True-Strain curve is used. The problem is that this part of the curve is too short to perform a best fit on it and get a good accuracy of the material behavior during the higher plastic strain range. To bypass this shortcoming, the ARAMIS imaging system (see Sect. 5.1.3) is used while testing the unnotched specimen to evaluate with precision the strain at notch's root surface and the smallest cross-sectional area. With the loading given by the INSTRON 1137, and the cross-sectional area given by ARAMIS in function of time, the average stress at notch can be evaluated. This does not give however the exact true stress-true strain curve. In fact the stress at the notch's root surface is the highest stress in an axisymmetric specimen until necking or renotching begin, after which the maximum stress "transits" toward the axis. Therefore, parameters (A, B, and n) found with this curve serve as a starting point for FE iterations.

In this case, the smooth specimen is modeled and parameters are modified until the simulation represents approximately the shape and the surface strain measured by the ARAMIS imaging system.

For damage parameters D_1, D_2, and D_3, the use of the ARAMIS system is also required and the following approach (inspired from Bao and Wierzbicki [34]) will be used. The procedure is divided into six main steps:

1. Perform a series of tensile tests with different specimens shapes (unnotched and notched) and obtain force-displacement responses. Film each test with the ARAMIS system to monitor the strain at surface and to follow the evolution of the shape in function of time.

2. Perform in parallel numerical simulations of those tests.

3. Determine from the simulations the location of fracture initiation and displacement to fracture, u_f, for each geometries.

4. Calculate the evolution of the equivalent strain and the stress triaxiality at the fracture location (ϵ_{eq} vs u and σ_H/σ_{eq} vs u) for each case.

5. Determine the equivalent strain to fracture, ϵ_{eq}^f, and the average stress triaxiality for each case.

6. Plot the results from Step 5 in $\epsilon_{eq} - \sigma_H/\sigma_{eq}$ space and construct the limiting fracture curve.

The numerical procedure can be verified by comparing the strain to fracture obtained by FEM and the strain to fracture calculated obtained with equation 4.15.

4.1.3 Quasi-static torsional test

No torsional test in quasi-static mode is done in this study. Torsional test gives the strain to fracture for a null triaxial ratio . From Bao and Wierzbicki [34], torsional test leads to a shear fracture instead of the uniaxial tensile test that is more associated with the void growth fracture mode. Since the Johnson-Cook damage model is based on the last mode, it is of little use to accomplish quasi-static torsional test.

A quasi-static torsional test could be done to evaluate the error made by the Johnson-Cook model while simulating fracture under similar state of stress. A complete description of the quasi-static torsional testing is provided by Oess [28]. Only very few authors such as Wierzbicki [22] have developed specimens with specific geometry to induce shear fracture with a tensile test machine.

Von Mises factors

Two simple relations give the true stress from the shear stress and the strain from the shear strain:

$$\sigma = \sqrt{3}\tau$$

$$\epsilon = \frac{\gamma}{\sqrt{3}} \tag{4.17}$$

$$\dot{\epsilon} = \frac{\dot{\gamma}}{\sqrt{3}}$$

The above relations are valid only for isotropic materials. Note also that Bridgman and von Mises factors are valid with the assumptions of von Mises theory . Therefore, they are not restricting the Johnson-Cook behavior model because it is based on the same assumptions.

4.2 Dynamic

For dynamic characterization tests with strain rate from 10^2 to 10^4 s^{-1}, the most reliable apparatus are the Split Hopkinson bars: compression, tension, and torsion (Kolsky bar). At higher strain rates, other tests like the Taylor impact test are necessary, but the data analysis of those tests are much more complex. Most of the high strain rate apparatus are described in the section *High Strain Rate Testing* of reference [29]. Here, only Hopkinson bars are presented.

4.2.1 Split Hopkinson pressure bar

The split Hopkinson pressure bar (SHPB) and the two following modifications in tension and in torsion use the stress wave propagation to load a specimen at high strain rate. The specimen is placed between two long bars; the incident and the transmitted bars. A striker is lunched against the incident bar at a specific speed. This impact generates an elastic compressive wave travelling along the bar towards the incident bar-specimen interface, and a time-dependent strain $\epsilon_I(t)$ is measured by the strain gage A. Note that the strain gage on the incident bar is placed at the mid-point of the incident bar to be sure that the incident and the reflected waves are measured independently. When the incident wave reaches the incident bar/specimen interface, part of the wave is reflected back in the incident bar as a tensile wave,$\epsilon_R(t)$, and the rest is transmitted through the specimen. The compressive wave in the specimen is partly absorbed by plastic deformation and the rest is transmitted to the output bar. Gage B measures the transmitted time-dependent strain, $\epsilon_T(t)$.

With the signals of the two strain gages A and B and some predetermined parameters, the strain rate and the average stress can be calculated as

$$\frac{d\epsilon}{dt} = \frac{V_1 - V_2}{L} \tag{4.18}$$

where V_1 and V_2 are the velocities at the incident bar/specimen and specimen/output bar interfaces, respectively, and L is the length of the specimen. Velocity V_1 is the product of the longitudinal sound velocity (C_o) in the pressure bar and the total strain at the incident bar/specimen interface, which is $\epsilon_I - \epsilon_R$. Similarly, the velocity V_2 is equal to $C_o\epsilon_T$. In the development, ϵ_I, ϵ_T, and ϵ are all compressive strains, but are considered positive, whereas the quantity ϵ_R, which represents a tensile strain, is negative. Replacing V_1 and V_2 in equation 4.18, the strain can be rewritten as

$$\frac{d\epsilon(t)}{dt} = \frac{C_o}{L}[\epsilon_I(t) - \epsilon_R(t) - \epsilon_T(t)] \tag{4.19}$$

where the longitudinal speed of sound is

$$C_o = \sqrt{\frac{E}{\rho}} \tag{4.20}$$

The average stress on the specimen is

$$\sigma(t) = \frac{P_1(t) + P_2(t)}{2A} \tag{4.21}$$

where P_1 and P_2 are the forces at the incident bar/specimen and specimen/output bar interfaces, respectively, and A is the instantaneous cross-sectional area of the specimen. At the incident bar/specimen interface, the force is

$$P_1(t) = E[\epsilon_I(t) + \epsilon_R(t)]A_o \tag{4.22}$$

and the force at the specimen/output bar is

$$P_2(t) = E\epsilon_T(t)A_o \tag{4.23}$$

where E is the Young's modulus, and A_o is the cross-sectional area of the bar. Replacing equations 4.22 and 4.23 in equation 4.21, the average stress can be calculated from the strain signals measured by gages A and B.

$$\sigma(t) = \frac{E}{2}\frac{A_o}{A}[\epsilon_I(t) + \epsilon_R(t) + \epsilon_T(t)] \tag{4.24}$$

4.2.2 Split Hopkinson tensile bar

To be able to perform high strain rate tensile test and also to rupture the specimen, the Split Hopkinson tensile bar (SHTB)has been developped. This apparatus could be easily used with an ARAMIS imaging system with high speed cameras as done in the present study for quasi-static tensile tests (see Sect. 5.1).

However, for the time being, DRDC Valcartier does not possess any SHTB able to test solid specimen.

4.2.3 Torsional Kolsky bar

The torsional Kolsky bar, schematically represented in figure 4.5, uses a short-thin tube material specimen that is fixed between two bars. A stored load is released in the incident bar and produces a short rising torsional signal that propagates along the incident bar. When the load wave comes to the incident bar/specimen interface, a part of the signal is transmitted to the other bar (transmitter) through the specimen and the other part of the signal is reflected back. The average deformation of the specimen is determined by monitoring the incident, reflected and transmitted waves in the bars. Since they remain elastic during the whole test,then by the energy balance equation, it is possible to determine the energy absorbed by the specimen's deformation.

This apparatus is a modification of the simplified SHPB. Torsional Kolsky bar can be adapted to process material testing at temperature below and above the ambient temperature. It allows also to study localization of plastic deformation through the formation of adiabatic shear bands. In the present document, this testing apparatus is choosen to get the high strain rate parameter of the Johnson-Cook damage model, D_4. Torsion generates a triaxial pressure free stress state in the specimen. Thus, effects of strain rate alone on strain to failure can be observed.

Like the SHTB, the torsional Kolsky bar is able to load the specimen to rupture. The physics of torsional elastic waves differs from that of the longitudinal waves (tensile and compressive). There is no radial expansion like in the compressed specimen due to the Poisson ratio that adds radial stress. Lubrication of the bars/specimen interfaces is avoided, but torsional specimen are more complex since they need grips and precise

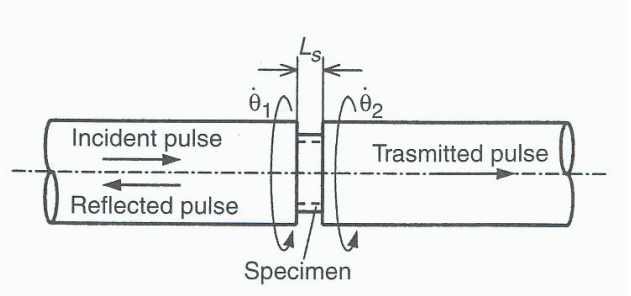

Figure 4.5: Schematic of the torsional Kolsky bar apparatus. Angular velocities of the ends of the specimen are denoted by $\dot{\theta}_1$ and $\dot{\theta}_2$, and the specimen's length is L_s.

machining. The beginning of the transmitted signal can be delayed by a loose in the grips for example. Torsional waves undergoe no geometric dispersion in contrast with compressive and tensile waves. Thus, a torsional pulse speed is not affected by its frequency when it travels along an elastic bar in its primary mode. Hence, careful attention should be taken during the application of the method used to initiate the torsional pulse. Some Kolsky apparatus use pulse initiated by detonation for sharp rise of the pulse. This method leads often to a noisy signal, which is not smoothed out as explained previously. The stored-torque method provides potentially higher strain, which is more appropriate to the present study since it is desired to bring the specimen to failure.

Calculation of the shear strain rate, strain and stress

Kolsky [35] determined the average shear strain rate and the average shear stress in the specimen by the same way as it was done for the SHPB. The average shear strain rate, $\dot{\gamma}_s(t)$, in the specimen can be written as

$$\dot{\gamma}_s(t) = \frac{c}{L_s}\frac{D_s}{D}(\gamma_T(t) - [\gamma_I(t) - \gamma_R(t)]) \tag{4.25}$$

where $c = \sqrt{\frac{G}{\rho}}$ is the shear wave velocity, L_s is the specimen gage length, D is the diameter of the Kolsky bar, D_s is the average diameter of the specimen gage length, and $\gamma_{T,I,R}(t)$ are respectively the shear signals measured during the passage of the transmitted, incident, and the reflected torsional waves.

Kolsky has also shown that the transmitted pulse provides a direct measurement of the average shear stress in the specimen, $\tau_s(t)$. This stress is given in term of the

torque in the thin-walled tube and is expressed as:

$$\tau_s = \frac{2M_s}{(\pi D_s^2)t_s} \tag{4.26}$$

where t_s is the wall thickness, and M_s the average torque whose equation is developed in the following sub-section. The average torque can be calculated from the torques measured at both ends of the specimen.

$$M_s = \frac{1}{2}(M_1 + M_2) \tag{4.27}$$

where M_1 and M_2 are the torques on the specimen ends in contact with the incident bar side and the transmitted bar side, respectively.

$$M_1 = G(\gamma_I + \gamma_R)\pi\frac{D^3}{16} \tag{4.28}$$

$$M_2 = G\gamma_T\pi\frac{D^3}{16} \tag{4.29}$$

Equations 4.25 and 4.26 provide average strain rate and stress in the specimen as a function of time. By integrating the strain rate in time , the stress-strain curve can be obtained.

Torque in a thin walled tube

The specimen placed between the incident and the transmitted bars is a thin walled cylindrical tube. While the bars remain in the elastic domain, the specimen of smaller radius undergoes plasticity at high strain rate. Thus, the thin part of the specimen illustrated in Fig. 4.6 is deformed under adiabatic shear loading.

According to the exact theory, the shear stress, $\tau_{\theta z}$, varies linearly with the radius and has its maximum value at the outer radius:

$$(\tau_{\theta z})_{max} = \frac{M_t r_o}{\frac{\pi}{2}(r_o^4 - r_i^4)} \tag{4.30}$$

For the calculation of numerical values corresponding to the strain rate, strain and shear stress fields, we use the approximation theory that states that the shear stress is uniformly distributed across the wall thickness. From equations of Fig. 4.7 the shear stress across the thickness can then be approximate as

$$\tau_{\theta z} = \frac{M_t}{2At} = \frac{M_t}{\frac{\pi}{2}(r_o + r_i)^2(r_o - r_i)} \tag{4.31}$$

where M_t is the torque supported by the transmitted bar. In our case, the ratio $r_i/r_o = 0.97$, hence the error between the exact theory and the approximation is 1.4%. Thus, the approximation of uniformity of the shear stress across the wall thickness is adequate.

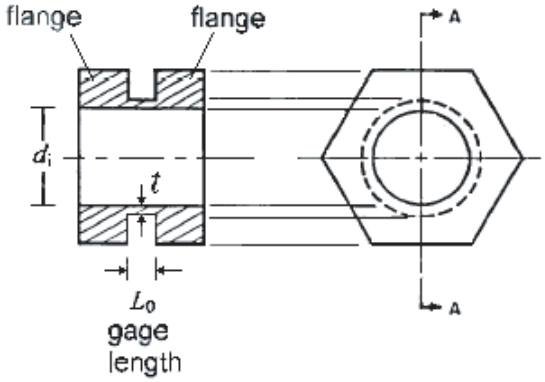

Figure 4.6: Details of the thin-walled specimen (here with hexagonal flanges). t and L_0 are the thickness and the length respectively of the gage zone of the specimen.

Shear band

In contrast with the stress and also with the strain across the thickness, the shear strain along the gage length is uniform only until a shear band begins. This instability acts as the necking process during a tensile test. In the first phase, the strain develops uniformly in the whole gage length until a defect in the specimen makes the strain converge in its region. At this instant, the stress begins to fall rapidly and the temperature grows in the shear band region. By an imaging system, Fellows and Harding [36] demonstrate the concentration of strain in a narrow region (see Fig. 4.8. From the instant at which the strain begins to concentrate around an assumed defect till the fracture, the shear band becomes narrower and propagates around the specimen. The study of Fellows and

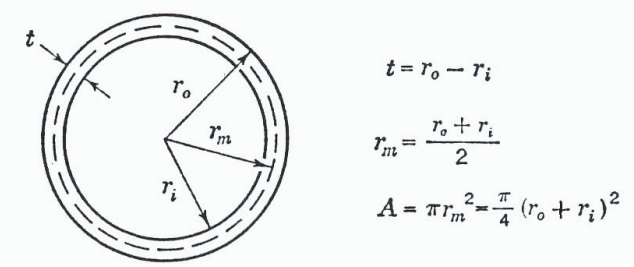

Figure 4.7: Geometrical description of a thin-walled tube of thickness t, mean radius r_m, and area A.

Harding shows clearly the difference of level between the average shear strain measured by the Kolsky bar, the shear strain in the shear band and the shear strain in the rest of the specimen's gage. Liao and Duffy [37] also use an imaging system to evaluate the local strain over the gage length and came out with similar conclusions as Fellows and Harding

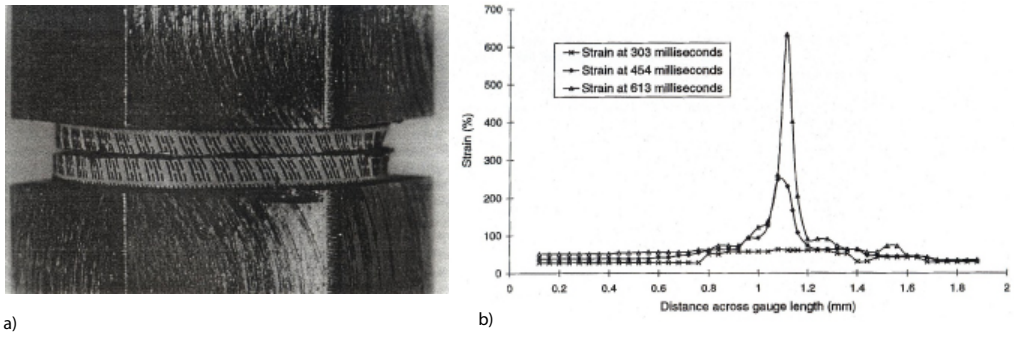

Figure 4.8: Localization of plastic deformation during high strain rate torsion testing of rolled homogeneous armor. a) Specimen B6 after fracture, b)Strain versus gage length of the specimen B6 at 303, 454, and 613 milliseconds. (taken from [36])

Hartley, Duffy and Hawley [38] measured the temperature profile along the specimen gage length during a torsional Kolsky test with an infrared detector. They have observed a rapid rise of the temperature in a thin region of the gage (shear band) synchronised with the reach of the maximum stress until the beginning of the fracture propagation, after which the temperature goes down. Since the only heat source here is the deformation work, the temperature measured by Hartley, Duffy and Hawley can be directly linked to the strain level in the specimen. Hence, the observations made by Hartley et al. confirm the one made by Fellows and Harding that the torsional Kolsky bar apparatus measurements give only average values. This is not new, but in the present context of material characterization, it is of great importance to know the exact state of stress in the specimen, especially at rupture. Thus, data such as strain to fracture should not be taken from! the torsional Kolsky bar instrumentation. Imaging system like the one used by Fellows and Harding could be used alone or combined with an infrared detector (like the one used be Hartley and al.) and/or FEM. For FE modeling of the specimen in torsion, the Johnson-Cook models are well suited for it, since they take into account the effects of strain rate and high temperature on hardening and fracture.

Note that a stored-torque torsional Kolsky bar is presently being assembled in the material laboratory of DRDC Valcartier. For material testing to rupture at higher strain rates than $10^4\,s^{-1}$, hat specimens can be used with a SHPB [39]. Mason and Worswick [40] performed punching-shear experiments (very similar to hat specimens

compression testing) at shear strain rates up to $45000\,s^{-1}$.

4.3 High temperature

As it is explained in Section 3.1.2, if the high temperature parameters (m and D_5) are used, the test should be done at high strain rate. Therefore, this section only suggests high strain rate apparatus specially modified to impose high temperature conditions. Most of it are based on one of the three split Hopkinson bar types. Note that such test have not been pursued in the present study.

High strain rate testing at high temperature can be divided into two categories. The first consists into heating the specimen and try to minimize the heat rise in the rest of the apparatus (mainly incident and transmitted bars). The second demands the monitoring of temperature gradient in the bars to be able to correct the results obtained if necessary.

The first approach is more suited for compressive tests, since there is no mechanical link other than simple contact between specimen and bars. The specimen can then be heated by a furnace to the right temperature and then the bars are placed into contact with the specimen shortly before the test beginning. If the contact is sufficiently short, the gradient can be neglected. Franz et al. [41] have conducted tests using this method at temperatures up to $1000\,°C$. With tensile or torsional Hopkinson bars, different way of heating should be used, since the bars need to be attached during the heating of the specimen. Thus high intensity localized heating device are used to avoid as much as possible the heating of the bars. For tensile testing, Rosenberg et al. [42], and Shazly et al. heated their specimens by inducting heating coil. Inserts can be placed between bars and the specimen. They isolate bars from the heated specimen. The! imped ance of those inserts should be as much as possible independent in temperature. Gilat and Wu [44] used titanium inserts for torsional Kolsky bars testing at temperatures ranging from room temperature to $1000\,°C$. Gilat and Wu used little burners to heat up the small gage length of torsion specimens.

The second approach allows thermal gradient in bars, but considers its effect on results. Gilat and Wu [44] listed the principal articles using this method for all three Hopkinson bars types.

Chapter 5

Experimental results

5.1 Quasi-static tensile tests

The aim of the tensile tests is first to obtain the true stress-true strain curve of the unnotched specimen. It is also to determine the strain to fracture at different states of stress. The state of stress depends on the specimen geometry (by example notch radius). Aluminum 5083 MIL-A-46027G (MR) and armor steel 4043 RHA MIL-A-12560G (MR) are tested. Since the state of stress at the center of the specimen is unmeasurable directly, FE modeling must be done in parallel to evaluate it. Therefore, every tests are filmed so as to be able to confirm the evolution of the shape with the FEM. This section describe the first set of tests done with a simple camera at 30 frames/second, and the second set done with the ARAMIS imaging system . The second set helps to confirm observations from the first set of tests.

5.1.1 Specimens description

RHA 4043 steel and aluminum 5083 specimens come from a 3/4, and 1 inch thick plates, respectively. Four different geometries are tested. Figure 5.1 shows a picture of the four geometries tested. The technical drawings can be found in Appendix A. Table 5.1 shows the important geometric parameters of the different samples. Specimens are cut in rolled aluminum and steel plate as shown in Figure 5.2, with the axis oriented in the rolling direction.

Table 5.1: Specimen dimensions

Specimens	R (mm)	Φ_0 (mm)	Φ_{Notch} (mm)
Unnotched	-	8	8
A	12	15	8
B	6	15	8
C	4	15	8

Figure 5.1: Four different RHA steel specimens

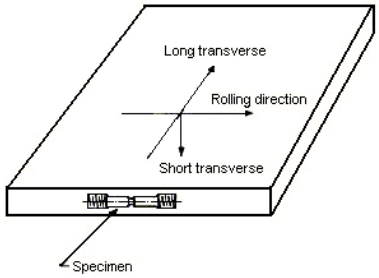

Figure 5.2: Cutting direction of aluminum and steel specimens in rolled plates.

5.1.2 Tensile test machine and data acquisition system

Tensile tests are performed using the servo-mechanical Instron 1137 of the Material Laboratory of DRDC-Valcartier. This model is supposed to have a crosshead speed range of 0.05 to 500 mm/min, and a frame stiffness, K_m, of 140 kN/mm, [45]. The apparatus have been calibrated by an independent firm in 2004. An extensiometer is used with the unnotched specimens tested at a speed of $2mm/min$ without the ARAMIS imaging system . The loading and the top screwdriven head displacement are sampled at $6Hz$.

To approximate the shape of the sample during test (for FEM correlation) a ELMO camera model PTC-100S has first been used at $30frames/sec$ to film each tests mainly for the shape monitoring of the specimen. The frequency could be easily reduced to one or two frames/second, because of the quasi-static nature of the phenomenon. The use of the camera shows an unexpected large global vertical movement of the specimen compared with its total extent, especially with the RHA steel specimens. This observation brings few questions about the INSTRON 1137 and its stiffness. Because the extensiometer could only be use till the beginning of the plastification, and not during the whole test duration, the nett cross-head displacement can not be evaluated using the extensiometer. The use of the ARAMIS system allows the evaluation of the

deformation undergone by the tensile test machine by measuring the displacement at both specimen's ends.

Normally, the tensile test machine is considered infinitely stiff compared with the material tested, thus most of the displacement imposed to the machine's screwhead is transmitted to the specimen's top head. Here, it is not the case, since high strength armor plate material are tested. The tensile test machine extends considerably during testing. Figure 5.3 shows a rigidity model of the tensile test machine-specimen system. Equation 5.1 gives the system machine-specimen stiffness, K_{syst}.

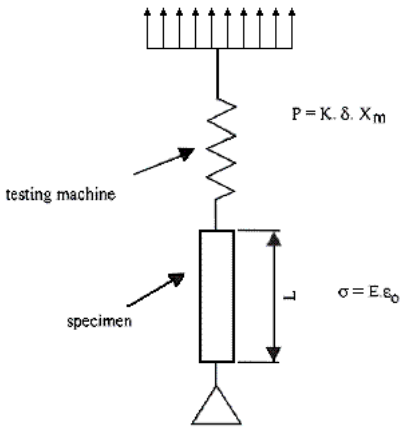

Figure 5.3: Tensile test machine-specimen rigidity model.

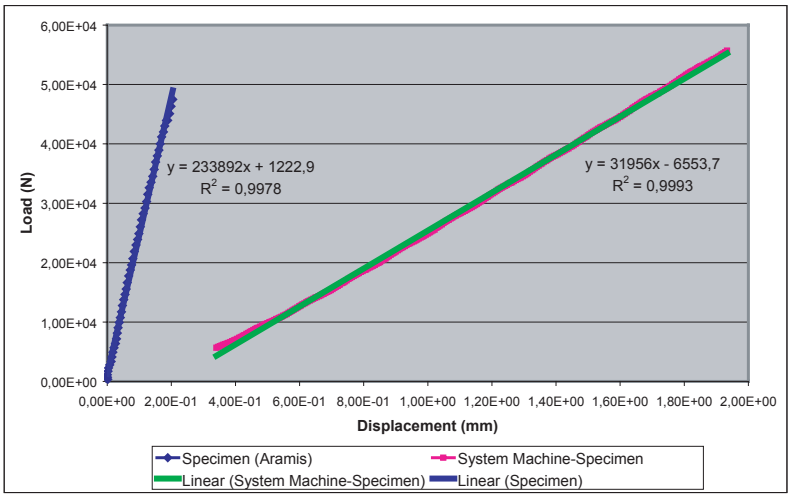

Figure 5.4: Linear stiffness curves of the specimen, and of the system machine-specimen.

$$\frac{1}{K_{syst}} = \frac{1}{K_m} + \frac{1}{K_{specimen}} \tag{5.1}$$

where $K_{specimen} = (\frac{1}{E}\frac{L}{A})$ is the specimen linear stiffness, L, and A its length and cross-sectional area, respectively. The system stiffness can also be extracted from a load versus displacement curve.

Figure 5.4 shows two curves, one is the system displacement (considering screwhead displacement). To obtain the specimen's stiffness when its Young modulus is unknown, the same kind of curve can be drawn for the specimen alone. To consider only the specimen, the contribution of the low part of the machine must be subtracted. The second curve of Fig. 5.4 shows the difference of displacement between the two specimen's ends. Now that rigidities of the specimen and the whole system are known ($K_{specimen} = 233892\,N/mm$ and $K_{syst} = 31956\,N/mm$), with Eq. 5.1 the machine's rigidity is; $K_m = 37013\,N/mm$, which is less than 30% of the given value from INSTRON. This even larger softness causes large difference in displacement between the specimen's top end and the srewdriven head, and the down head can not be considered fixed anymore.

5.1.3 ARAMIS Imaging system

ARAMIS^{TM} is a photogrammetric system from GOM mbH. It is suited for 3D deformation measurements of a loaded structure at static, quasi-static, or dynamic regime. The version of this system used in the present study is the ARAMIS HS. Table 5.2 presents its general characteristics. Note that images can come from any other cameras like high speed camera, the only restriction for the use of ARAMIS is the specimen preparation.

Table 5.2: ARAMIS HS general characteristics

Camera CCD	1280x1280 pixels
Measuring area	mm^2 up to m^2
Frame rate	up to 8000 Hz
Strain measuring range	0.1% up to >100%
Strain measuring accuracy	up to 0.02%

Principle of operation

Two CCD cameras (calibrated prior to measurements) capture the loaded specimen from different angles (from 15 deg to 35 deg between camera's axis). Figures 5.5 and 5.6 shows Aramis from the side and the back of the tensile test machine. A random pattern drawn on the specimen is initially captured and split in facets by the image processing. The following paragraph describes in details the specimen's preparation. In the present characterization tests, each facet is 15 pixels wide with an 8 pixels overlapping area. Figure 5.7 presents an image from the "left camera" of the specimen

RHAUN07 at the test beginning. The image is zoomed in at a pixel level. It shows four facets, from them two are overlaying. Each picture of the film has a size of 1280x1280 pixels. The processor computes one 3D coordinate point at the center of each facet. If the area filmed is about 50x50mm, as for specimens ALUN07 and RHAUN07, it gives a 3D position measurements at every 7 pixels or at every 0.27 mm on the view plan. During loading, solid movement and local deformation occur. The drawn pattern follows the specimen and the processor recognizes the pattern's displacement and deformation. After that, the spatial coordinates in function of time and thus the deformation and the plane strain tensor over all loading stages can be sketched or exported.

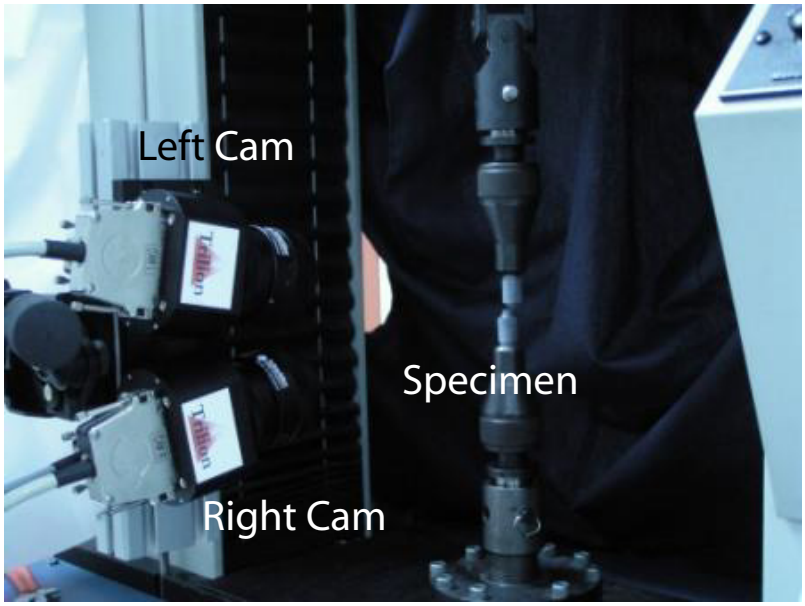

Figure 5.5: Side view of Aramis and the tensile test specimen.

Specimen's preparation

A stochastic pattern is applied on the specimen with spray paint cans. The paint must be matt to avoid shiny surfaces. In this study, a thin layer of matt black metal paint is applied firstly on the specimen. The best pattern for the ARAMIS's algorithm is highly contrasted, there should be about five spots visible per facets, and each spots should be from 3 to 5 pixels wide. In this study, a fume of white paint has then been applied over the dried black paint. Little spots are obtained by gently pressing the spray button. Figure 5.8 shows an unnotched specimen prepared for measurement with the ARAMIS system. Figure 5.7 shows few facets of the RHAUN07 specimen at the beginning of the tensile test.

Figure 5.6: Back view of Aramis and the tensile test specimen.

5.1.4 Tensile tests results

Behavior parameters

Without the ARAMIS imaging system , the curve on Figure 5.9 is obtained. The preliminary parameters obtained with it would be: $A = 1193E^6 Pa$, $B = 7.0E^9 Pa$, and $n = 0.7322$. Parameter B is very high as expected, since it only takes into account the True stress-True plastic strain before necking. The slope is then also too high.

By using the ARAMIS system, the whole True stress-True plastic strain curve can be considered. Figure 5.10 shows the resulting curve in a log-log graph. The curve on it shows a higher slope at the beginning that stabilizes on the second half. Table 5.3 list the parameters found and that serve for the simulations described in Chapt. 6, which give the first three damage model's parameters.

Table B.1 enumerates the tensile test results for the RHA steel 4043. In this table,the loading values come from the Instron 1137 output, while the other values come from direct measurements on the specimens. Graphics of Chapter 6 gives more results from the imaging system ARAMIS for FEM matching.

5.2 Torsional tests at high strain rates

Torsional testings with a Kolsky bar apparatus have been carried out by the Mechanical Engineering Department, University in Winnipeg (MUW), Manitoba. The same steels as in Section 5.1 have been tested at different strain rates ranging from about $900\,s^{-1}$

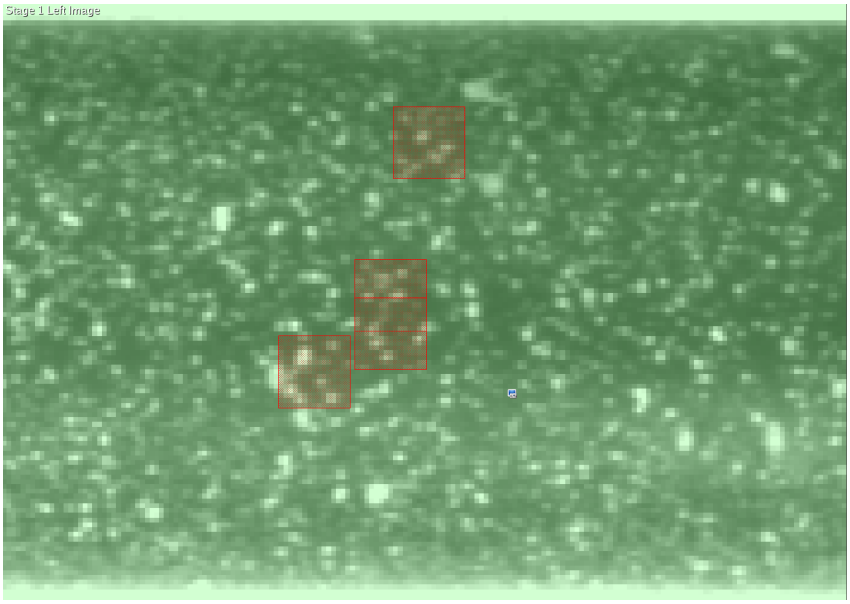

Figure 5.7: Numerized image showing a part of the computed zone of the specimen RHAUN07. There is 4 facets in red.

to $1500\,s^{-1}$. Only one test has been performed for each strain rate. Unfortunately, data were unusable for many reasons out of the author's control. Thus, no dynamic parameter are determined in the present study. Here again, the importance of being autonomous in the parameters determination is clear. Fortunately, equipments necessary for the high strain rate Johnson-Cook parameters determination will be available in October 2006 at the DRDC Valcartier.

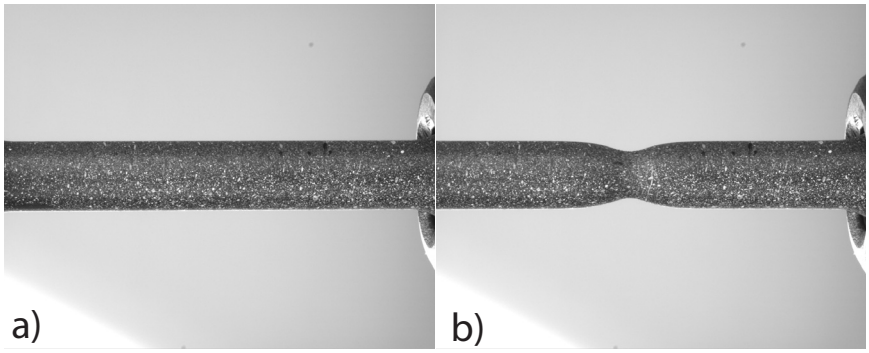

Figure 5.8: Specimen RHAUN08 filmed by the so called "left camera" (view from the top) of ARAMIS, a) at 8 seconds, and b) at 210 seconds.

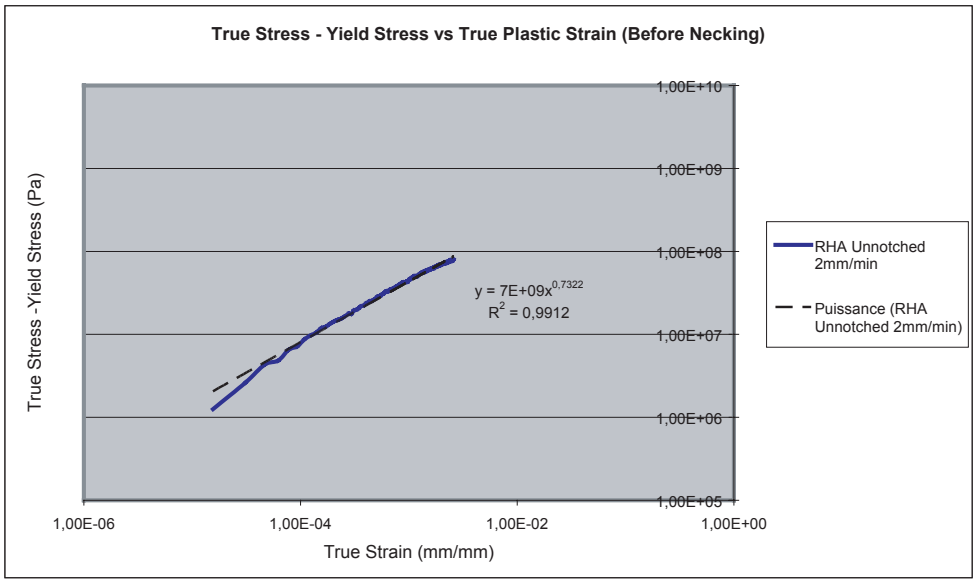

Figure 5.9: Log-log graph of the True stress-Yield Stress versus True plastic strain derived from INSTRON 1137's data. Only data between the yield stress and the maximum stress are considered

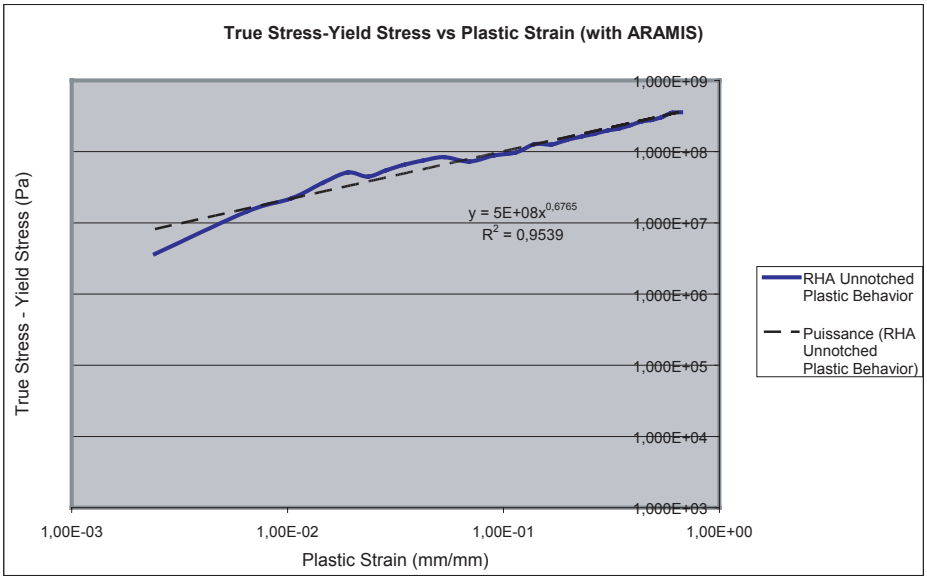

Figure 5.10: Log-log graph of the True stress-Yield Stress versus True plastic strain derived from INSTRON 1137 and ARAMIS's data. Data between the yield stress and fracture are considered

Table 5.3: RHA steel static Johnson-Cook parameters determined.

Parameter	Value
A (Yield Stress)	$1190E^6$ Pa
B (Hardening Factor)	$5.0E^8$ Pa
n (Hardening Coeff.)	0.6765

Chapter 6

Numerical

6.1 Quasi-static damage model's parameter determination

As explained in previous chapters, the first three Johnson-Cook damage parameters link the strain to fracture to the state of stress at fracture. Since the state of stress is impossible to measure at the center of a uniaxial specimen at fracture and because Bridgman analytical model's evaluation carries large errors (see 4.1), the solution tried here is to model the tensile tests described in Chap. 5. The following presents the finite element modeling of the tested four specimen's geometries. For a reason of lack of time, no numerical analysis of the aluminium 5083 have been done.

The present quasi-static simulation is done using an explicit code with a control of the timestep instead of using a implicit code. The goal of the global project including this Master of Science thesis is to modelise high strain rate phenomena with the J.-C. model in its explicit form. The purpose of this is to test the good implementation of the Johnson-Cook model in Ls-Dyna in its explicit form.

6.1.1 Tensile tests modeling

Figures 6.1, and 6.2 present the four tensile specimens meshed with 8-noded solid elements. Unnotched, 12 mm, 6 mm, and 4mm specimen's meshes were generated and comprised 15360, 12880, 12995 and 12880 elements, respectively. The material model used is of course the Johnson-Cook visco-plastic model. The behavior model's parameters of the RHA steel not determined in chapter 5 come from reference [2], and are not very relevant in this quasi-static, and isothermal simulation. Note that the unit convention adopted for this study is the "kilogram, meter, second." The following sub-sections present LS-Dyna cards used for the quasi-static tensile test models. In general variables left to default values will not be discussed in the cards description, and the reader should refer to the LS-Dyna user's manual [17].

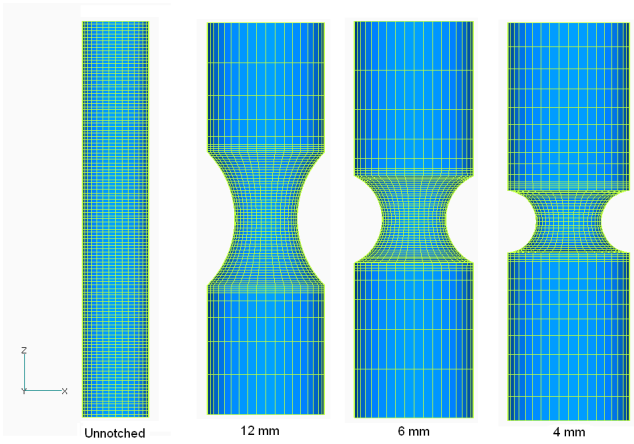

Figure 6.1: Four meshed tensile test specimens: Unnotched, 12 mm, 6 mm, and 4 mm radius notch.

*CONTROL_TERMINATION

This card stop the job lunched when it reach the value of the variable "ENDTIM." The time termination changes depending on the modeled specimen .

*CONTROL_TERMINATION				
$ ENDTIM	ENDCYC	DTMIN	ENDENG	ENDMAS
85.0	0	0.0	0.0	0.0

*CONTROL_TIMESTEP

This card is used to set the structural time step size using different options. "TSSFAC" is the time step scale factor. During the solution, LS-Dyna loop on every element to find the smallest time step, which is scaled by the factor "TSSFAC." "DT2MS" is used here since a quasi-static loading is modeled with an explicit code. This constant scale down the mass to reduce the computed sound speed. It rises the time step, and thus reduce rapidly the time computation. This parameter must be used carefully. The scaling factor has no bad effect on the simulation as long as the kinetic energy is few order less than the internal energy (less than 1%). Kinetic energy over internal energy versus time curves for each specimen are presented in figure 6.3, since the kinetic energy is well under 1% of the internal energy the value of "DT2MS" is well set.

*CONTROL_TIMESTEP							
$ DTINT	TSSFAC	ISDO	TSLIMT	DT2MS	LCTM	ERODE	MSIST
0.0	1.0	0	0.0	0.008	0	0	0

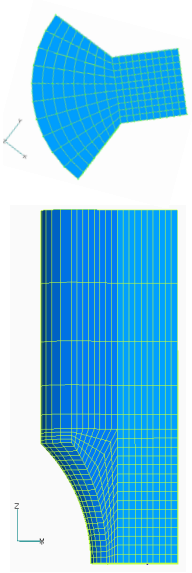

Figure 6.2: Tilted and top views of the 12 mm specimen mesh cut.

***PART**

The purpose of this card is to define parts by combining: section (SECID), material (MID), equation of state (EOSID) as well as the hourglassing information (HGID).

```
*PART
HEADING
$ PID   SECID   MID   EOSID   HGID   ADPOPT   TMID
2       2       2     1       0      0        0
```

***SECTION_SOLID**

This card is used to define the properties of the solid continuum. The section ID (SECID) is used by the *PART card for cross reference, the element formulation (ELFORM) option was set for constant stress solid elements (value= 1).

```
*SECTION_SOLID
$ SECID   ELFORM
2         1
```

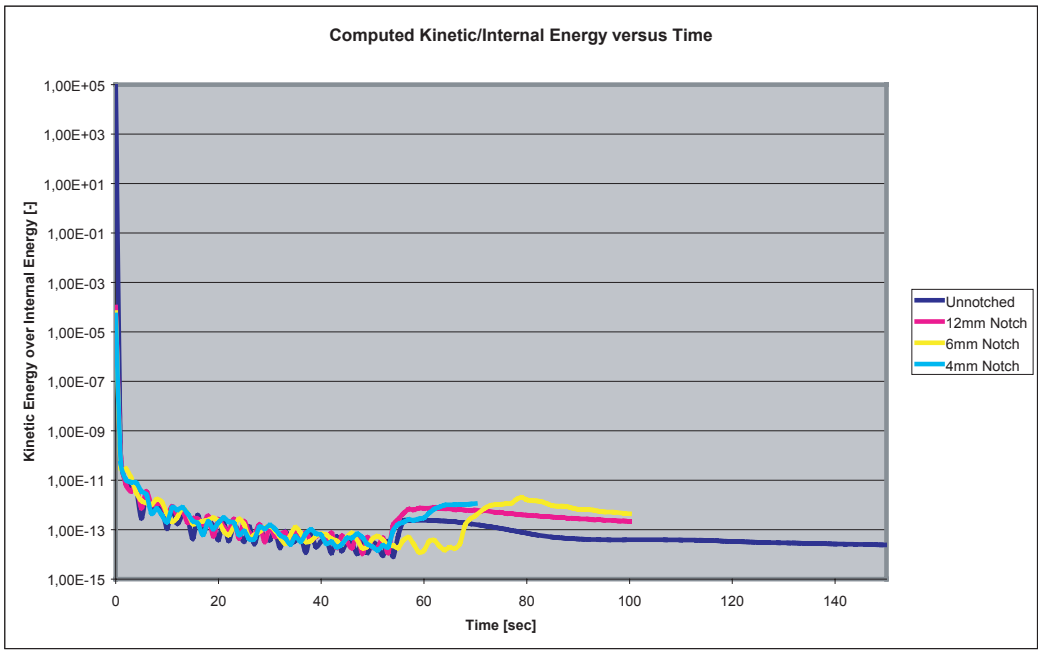

Figure 6.3: Computed kinetic energy over internal energy for each simulated specimens versus time.

*MAT_JOHNSON_COOK

In this card the material constitutive model is chosen and variables defined. The Johnson-Cook model is explained in Chap. 3. For the full description of the card input variables the reader should refer to LS-Dyna user's manual [17]. Static parameters (A, B, and n) come from experimental tests of Chap. 5.

*EOS_GRUNEISEN

The equation of state card relates the density and internal energy of the material with pressure. The Grüneisen EOS with cubic shock velocity defines pressure for compressed material as explained in Sect. 3.2.2. For the full description of the card input variables the reader should refer to LS-Dyna user's manual [17].

*DEFINE_CURVE

The purpose of this card is to edit a piecewise-linear curve referred by other cards, in which the abscissa represents time. Here, the only curve created is used to set the loading speed imposed at the top head of specimens (ordinate value), and that varies with time. "LCID" is the curve ID, "OFFA" and "OFFO" are offsets for abscissa and ordinate, respectively. Subsequent rows define curve amplitude (O1), at at precise time

```
*MAT_JOHNSON_COOK
$ MID       RO          G          E          PR      DTF     VP
2           7850.0      77.3e+9    206.8e+9   0.294   0.0     0.0

$ A         B           N          C          M       TM      TR      EPSO
1193.0e+06  500.0e+06   0.6765     4.35e-03   1.17    1723.0  295.    1.0

$ CP        PC          SPALL      IT         D1      D2      D3      D4
477.        0.          0          0          0.      0.      0.      0.

$ D5
0.0

*EOS_GRUNEISEN
$ EOSID   C      S1     S2    S3    GAMMA    A     E0
1         4570   1.49   0.0   0.0   1.16     0.0   0.0

$ VO
1.0
```

(A1).

```
*DEFINE_CURVE
$ LCID   SIDR      SFA   SFO   OFFA   OFFO   DATTYP
1        0         1.0   1.0   0.0    0.0    0

$ A1     O1
0.0      1.385E-6
67.0     1.385E-6
77.0     3.25E-5
...      ...
```

Since the INSTRON 1137 tensile test machine is stretching noticeably, the displacement applied to its screwhead can not simply be imposed to the up head of the specimen during simulation. Figure 6.4 presents displacement imposed to each specimen considering the stretching of the INSTRON 1137. Those displacements have been evaluated by the data analysis of the ARAMIS imaging system (see Sect. 5.1.3).

*BOUNDARY_PRESCRIBED_MOTION_NODE

This card defines an imposed nodal motion (velocity, acceleration, or displacement). The first parameter "NID" set the node id at which the motion is imposed. The

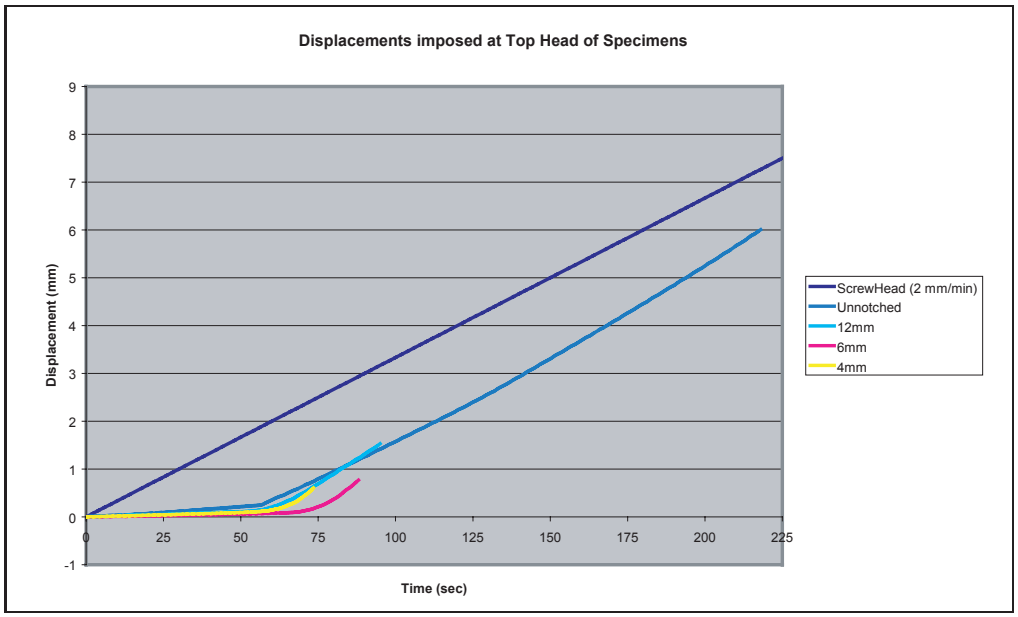

Figure 6.4: Four displacements imposed at the top of specimen are compared with the srewhead displacement.

parameter "DOF" sets the degree-of-freedom imposed to the concerned node. Here 3 means a strictly z-translational motion is imposed. "VAD" defines the type of motion imposed (here it is set to 0: velocity). The motion is defined by a "*DEFINE_CURVE" called by the parameter "LCID." "SF" is a scale factor to the load curve.

*BOUNDARY_PRESCRIBED_MOTION_NODE

$ NID	DOF	VAD	LCID	SF	VID	DEATH	BIRTH
3120	3	0	1	1.0	0	1.0E+28	0.0
3121	3	0	1	1.0	0	1.0E+28	0.0
3122	3	0	1	1.0	0	1.0E+28	0.0

...

*BOUNDARY_SPC_NODE

This card constrains node listed under variable "NID". "DOFX, Y, Z" represent translational constraints in x, y, and z direction, respectively, and are set to 0 when free, or to 1 when constrained. Rotational constraint variables "DOFRX, Y, and Z" work the same way. In the quasi-static tensile tests modeling, the present card is used to fixed the down head of the specimen.

*BOUNDARY_SPC_NODE

$ NID	CID	DOFX	DOFY	DOFZ	DOFRX	DOFRY	DOFRZ
10537	0	1	1	1	1	1	1
10538	0	1	1	1	1	1	1
10539	0	1	1	1	1	1	1

...

***NODE**

It lists nodes and their respective 3D coordinates that compose the mesh.

*NODE

$ NID	X	Y	Z	TC	RC
50	0.004163	0.002835	0.00645	1	1
51	0.004363	0.002902	0.00645	1	1
52	0.004453	0.002944	0.00645	1	1

...

***ELEMENT_SOLIDE**

It defines 3D elements by their nodes (here eight nodes) listed on the same row. "PID" tells the part in which this element belongs.

*ELEMENT_SOLIDE

$ EID	PID								
581	2	7139	8511	594	475	6908	8305	303	6907
582	2	475	594	595	476	6907	303	304	245
583	2	476	595	596	7136	245	304	305	246

...

6.1.2 Quasi-static simulation results

Before any results are taken into account, the kinetic energy level is compared to the internal energy level (see Sect. 6.1.1). Here for the four specimens tested, the kinetic energy is at least 11 orders less than the internal energy amplitude. Thus the mass scaling factor is adequate.

Figure 6.5 presents the progression of the specimen's diameter at notch center in function of time. Direct measurements, on tested specimens, of the diameter after fracture are added to each graphics. ARAMIS evaluation of diameter at the notch center is also included for the complete time interval of the test.

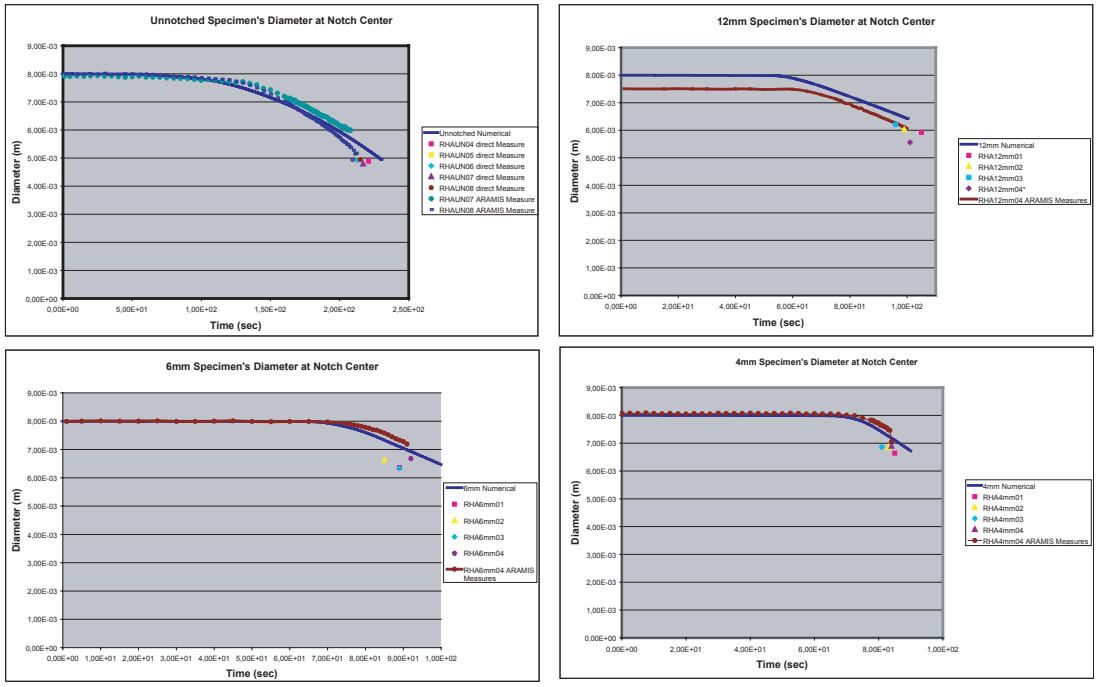

Figure 6.5: Four specimen's diameter at notch center of the modeled specimens, plus experimental measurements of the diameter after fracture of corresponding specimens, and ARAMIS measurement.

Figure 6.6 shows different strains at notch. Curves named "Numerical Plastic Strain " represent the effective plastic strain of an element on the notch surface. Curves built from ARAMIS measurements are added for comparison. In addition, direct measurements of the specimen's diameter gives a data point of the average fracture strain for each specimen.

6.1.3 Results analysis

Note that the 12mm notch specimen tested with ARAMIS had a different shape as it was supposed to be. Its diameter at the notch's root before testing was of $7.55mm$ instead of $8.00mm$. Since the loading curves come from the displacement difference between specimen's ends, which are calculated by ARAMIS, data analysis of the 12mm notch geometry are fastidious. Note also that the simulation results are very dependent from the displacement imposed, and thus the precision of measurements. Eventhough, ARAMIS measurements seems to fit with the measurements made after fracture.

Large strain seems to occur during the second before fracture of the notched specimens only. This would explain the gap observed between diameter at notch measured

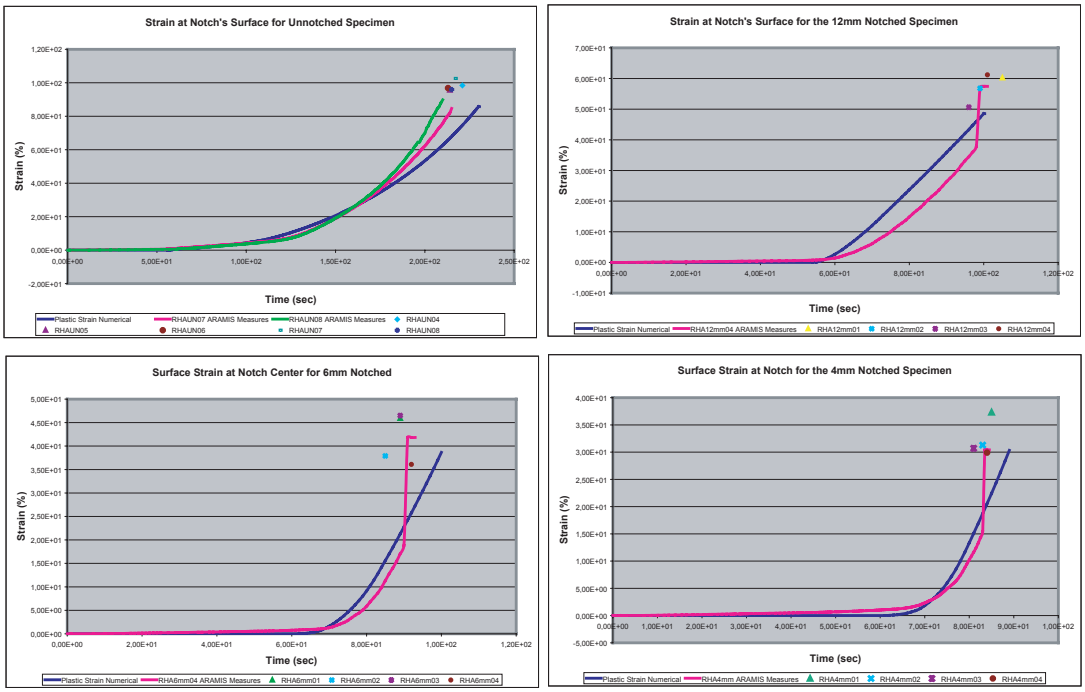

Figure 6.6: Four specimen's strain at notch surface of the modeled specimens, plus experimental measures of the average fracture strain of corresponding specimens, and ARAMIS measurement of surface strain.

with ARAMIS before rupture, and the direct measurements made on the specimens after rupture. Hopefully, from ARAMIS's data after rupture, this large deformation is mainly monitored by ARAMIS.

Tensile test simulation results seem to be close to the experimental measurements of the diameter made with ARAMIS, except for the final deformation that undergoes just before fracture. Since this large deformation seems to be closely associated with the specimen's break, the state of stress calculated by LS-Dyna could be taken as the state of stress at fracture of the specimen without making a large error on the rupture moment and state of stress.

6.1.4 Static damage parameters computation

When simulations are in good agreement with Aramis and direct measurements, the computed state of stress can be taken as the real one. Thus the post-processor gives the pressure and the equivalent stress for each specimens. The most strained element of each specimen must be found. This critical element is normally lying on the axis at notch root. Figures 6.7, 6.8, and 6.9 show one half of the specimens at rupture

time. Very low pressure (positive hydrostatic pressure), high level of plastic strain and also high level of equivalent stress are visible at center of the specimens. Note that specimen 12mm notched is not considered for reasons discussed in section 6.1.3. Figure 6.10 shows the graph of the computed triaxial ratio of the three specimens considered and their mean value. The mean value over the testing duration untill rupture is the triaxial ratio considered for the parameters determination, since one specimen's shape is taken globally as a constant triaxial ratio. The three data points obtained are drawn in figure 6.11, where the strain at fracture is the average value of the direct measurements made on each experiments (see Table B). To determine the three parameters $D1$, $D2$, and $D3$, a least mean square algorithm is applied between the three points and the model approximation. The three parameters found are in table 6.1, and a best fit curve (eq. 2.14) is drawn from these parameters on figure 6.11. The are also compaired with similar steel from Johnson and Cook [2] and from Rohr, Nahme and Klaus [46]. Note that it is not mention in [46] if they use any photogrammetrical system to characterise there material at quasi-static regime. From the data express in table 6.1, it can be seen that the present results are of the same order than the ones obtained by Rohr, Nahme and Klaus [46], at least for $D1$ which is the bottom limit at high triaxiality. By looking in [46], the figure 6 exposes the precision of the curve at low positive triaxiality. Considering only the error on the curve presented in [46], the results obtained in the present work would agree with for the three quasi-static damage parameters.

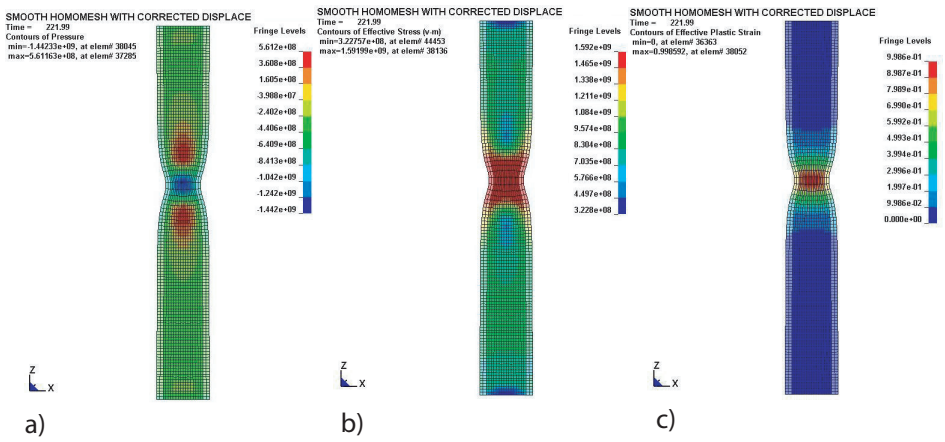

Figure 6.7: Section of the unnotched FE specimen, a) showing the pressure [Pa], b) the equivalent stress [Pa], and c) the plastic strain [-] at rupture time.

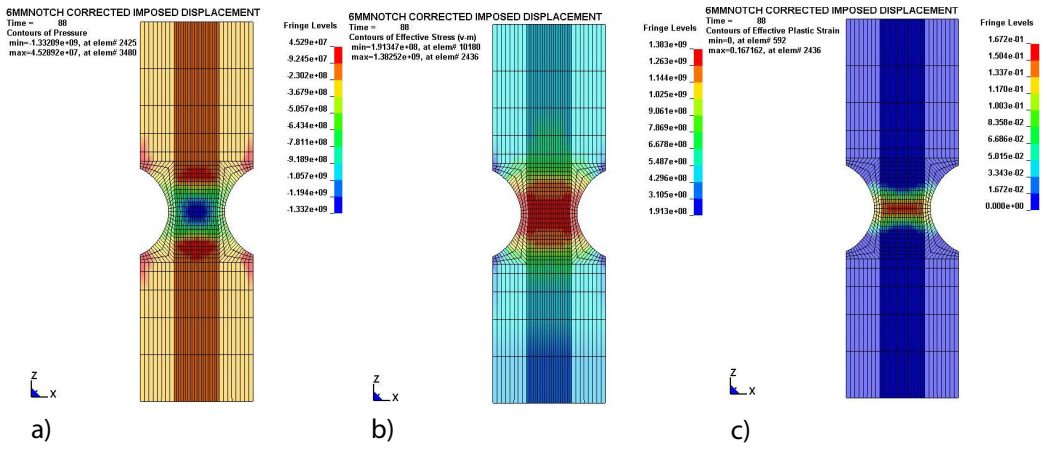

Figure 6.8: Section of the 6mm notch FE specimen, a) showing the pressure [Pa], b) the equivalent stress [Pa], and c) the plastic strain [-] at rupture time.

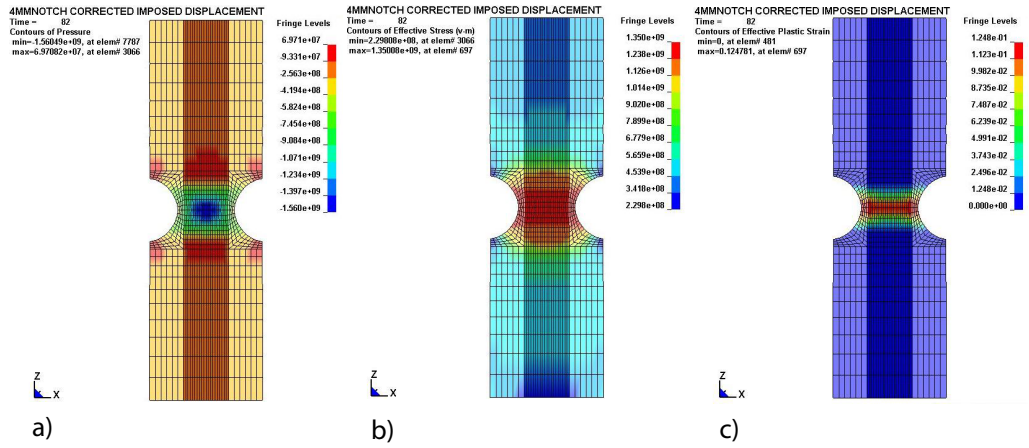

Figure 6.9: Section of the 4mm notch FE specimen, a) showing the pressure [Pa], b) the equivalent stress [Pa], and c) the plastic strain [-] at rupture time.

Table 6.1: Comparison of the RHA steel static damage Johnson-Cook parameters determined

Parameter	Present Analysis Values	J.C. [2]	Rohr [46]
D_1 (Void Nucleation Strain)	0.20839	0.005	0.48
D_2	7.20261	3.44	5
D_3	−5.44193	−2.12	−3.7

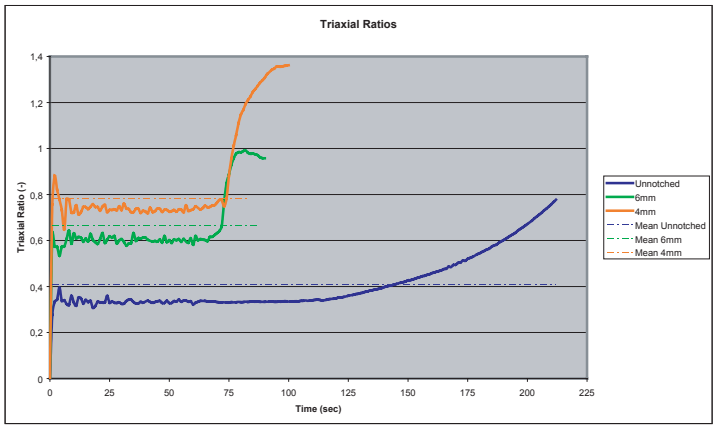

Figure 6.10: Graph of the triaxial ratio versus time and mean value for specimens unnotched, 6mm notch, and 4mm notch.

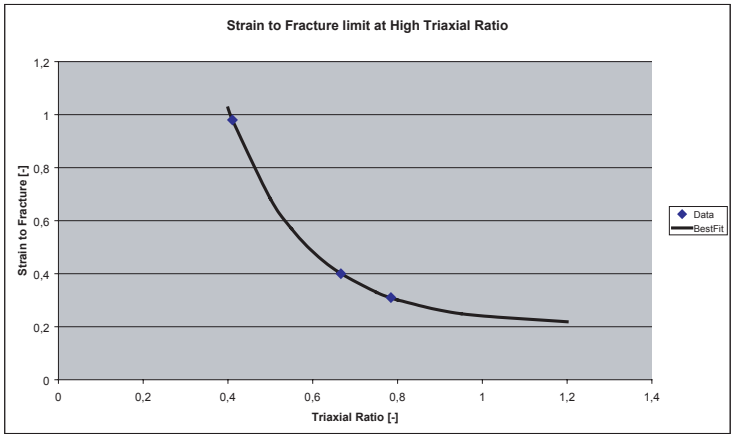

Figure 6.11: Strain to frature limit at high triaxial ratio for RHA steel.

Chapter 7

Summary and Conclusion

The following steps have been made to present the attempt to improve the characterisation method of the Johnson-Cook model.

- Introduction to the Johnson-Cook model by the CDM theory
- Presentation of the caracterisation technique proposed by the authors of the model
- Description of the experimental method necessary to make the characterisation
- From the first set of experimental, an improvement is proposed for the determination of the static parameters. This improvement include the use of the photogrammetric system ARAMIS.
- Simulation of the quasi-static tests with LS-Dyna are extensively described. These simulations are necessary to determine the three static damage parameters.
- Finally six new values for the static parameters are found and listed.

In conclusion, the characterisation method proposed by Johnson and Cook does not allow an easy determination of the parameters. To determine the three static constitutive parameters, the engineer stress-strain curve can not be used, since the valid part of the plastic curve is too short to represent the whole plastic range of a material. To determine the three static damage parameters, the triaxial ratio cannot be evaluated with precision with any analytic model like the Bridgman model. To solve these two problems, the photogrammetric system ARAMIS is used. It allows to track the local deformation field of a specimen for the whole time range (and by the way the whole plastic range). The static damage parameter are determined by comparing the deformation field measured by ARAMIS with the experimental test's simulation with LS-Dyna. When both are in good agreement, the triaxial ratio computed by LS-Dyna is assumed to be the real one and the static damage parameters can be! deter mined. The improvements make the determination of the parameters more accurate and easier.

Bibliography

[1] G.R. Johnson, W.H. Cook, *A constitutive model and data for metals subjected to large strains, high temperatures*, in Proceedings of the seventh International Symposium on Ballistic, The Netherlands, The Hague, 1983, pp. 541-547.

[2] G.R. Johnson, W.H. Cook, *Fracture characteristics of three metals subjected to various strains, strain rates, temperatures and pressures*, Engineering Fracture Mechanics Vol. 21, No. 1, 1985, pp. 31-48.

[3] G.T. Gray III, S.R. Chen, W. Wright, M.F. Lopez, *Constitutive equations for annealed metals under compression at high strain rates and high temperatures*, LA-12669-MS, January 1994.

[4] J. Lemaître, D. Krajcinovic, *Continuum Damage Mechanics Theory and Applications*, CISM Lectures, Springer, Berlin Heidelberg New York, 1987.

[5] J. Lemaître, R. Desmora, *Engineering damage mechanics: ductile, creep, fatigue and brittle failures*, Springer, Berlin Heidelberg New York, 2005.

[6] F.A. McClintock, *A Criterion for ductile fracture by growth of holes*, J. Appl. Mechanics, Vol. 35, 1968, pp 363-371.

[7] J.R. Rice, D.M. Tracey, *On the ductile enlargement of voids in triaxial stress fields*, J. Mech. Phys. Solids, Vol. 17, 1969, pp 201-217.

[8] P.W. Bridgman, *Studies in large plastic flow and fracture*, London: McGraw-Hill, 1952.

[9] B. Adams, *Simulation of ballistic impacts on armored civil vehicles*, Department of Mechanical Engineering of Eindhoven University of Technology, PhD thesis, MT 06.03.

[10] J.W. Hancock, A.C. Mackenzie, *On the mechanisms of ductile failure in high strength steels subjected to multi-axial stress-states*, J. Mech. Phys. Solids, Vol. 24, 1976, pp 147-169.

[11] M.J. Murphy, User's Guide for 2DJET Analysis of Shaped Charge, Livermore National Laboratory, UCID-21451, July 15, 1998.

[12] G. R. Johnson, *Materials Characterizations Involving Severe Dynamic Loading*, Proc. Army Symposium on Solid Mechanics, 1980, pp. 62-67.

[13] T.J. Holmquist and G.R. Johnson, *Determination of constants and comparison of results for various constitutive models*, in Journal de physique IV, Colloque C3, suppl. au Journal de physique III, Vol. 1, Oct. 1991, pp. 853-860.

[14] W.R. Rule and S.E. Jones, *A revised form for the Johnson-Cook strength model*, International Journal of Impact Engineering, Vol. 21, No. 8, 1998, pp. 609-624.

[15] P.S. Follansbee, *High-strain-rate deformation of FCC metals and alloys*, in Metallurgical Applications of Shock-Wave and High-Strain-Rate Phenomena, L.E. Murr, K.P. Staudhammer, and M.A. Meyers, Editions Marcel Dekker Inc., New York, pp. 451-479, 1986.

[16] D. Lesuer, *Experimental investigation of material models for Ti-6Al-4V and 2024-T3*, FAA Report DOT/FAA/AR-00/25, September 2000.

[17] LS-Dyna, *User's Manual*, Livermore Software Technology Corporation, Version 970, April 2003.

[18] R. G. Whirley, B.E. Engleman, J.I. Lin, *A nonlinear, explicit, three-dimensional finite element code for solid and structural mechanics - User Manual*, Lawrence Livermore National Laboratory Report UCRL-MA-10752, 1999.

[19] M.A. Meyers, *Dynamic behavior of materials*, John Wiley & Sons, New York, 1994.

[20] J. W. Hancock and D. K. Brown, *On the Role of Strain and Stress State in Ductile Failure*, J. Mech. Phys. Sol., vol. 31, 1983, pp. 1-24.

[21] G. Kay, *Failure Modeling of Titanium 6Al-4V and Aluminium 2024-T3 with the Johnson-Cook Material Model*, DOT/FAA/AR-03/57, September 2003.

[22] T. Wierzbicki, Y. Bao, Y.-W. Lee and Y. Bai, *Calibration and Evaluation of Seven Fracture Models*, International Journal of Mechanical Sciences, vol. 47, 2005, pp 719-743.

[23] Y. Bao, T. Wierzbicki, *On the Cut-Off Value of Negative Triaxiality for Failure*, Engineering Fracture Mechanics, Vol. 72, 2005, pp. 1049-1069.

[24] T. Nicholas and A. M. Rajendran, *High Velocity Impact Dynamics: Material Characterization at High Strain Rates*, Edited by Jonas A. Zukas, John Wiley & Sons, pp. 127-296, 1990.

[25] X. Teng, T. Wierzbicki, *Effect of fracture criteria on high velocity perforation of thin beams*, International Journal of Computational Methods, Vol. 1, No. 1, 2004, pp.171-200.

[26] G.R. Johnson, T.J. Holmquist, *Test Data and Computational Strength and Fracture Model Constants for 23 Materials Subjected to Large Strain, High Strain Rates, and High Temperature*, Technical Report LA-11463-MS, Los Alamos National Laboratory; 1989. (not in possession of the author)

[27] C.E.Anderson Jr., T.J. Holmquist, and T.R. Sharron, *Quantification of the effect of using the Johnson-Cook damage model in numerical simulations of penetration and perforation*, International Ballistic Symposium Vancouver, Vol.2, 2005.

[28] J.L. Oess, *Quasi-static torsional testing*, in ASM Metal Handbook, Vol. 8, 1985, Mechanical Testing, pp.145-148.

[29] Many authors, *High Strain Rate Testing*, in ASM Metal Handbook, Vol. 8, 1985, Mechanical Testing, pp.185-231.

[30] Y. Ling, *Uniaxial True Stress-Strain after necking*, AMP Journal of Technology Vol. 5, 1996, pp.37-48.

[31] G. La Rosa, G. Mirone and A. Risitano, *Effect of stress triaxial corrected plastic flow on ductile damage evolution in the framework of continuum damage mechanics*, Engineering Fracture Mechanics, Vol. 68, 2001, pp. 417-434.

[32] G. La Rosa, G. Mirone and A. Risitano, *Postnecking elastoplastic characterization: Degree of approximation in the Bridgman method and properties of the Flow-Stress/True-Stress Ratio*, Metallurgical and Materials Transaction A, Vol. 34, March 2003, pp. 615-624.

[33] M. Alves and N. Jones, *Influence of hydrostatic stress on failure of axisymmetric notched specimens*, Journal of the Mechanics and Physics of Solids, Vol. 47, 1999, pp. 643-667.

[34] Y. Bao, T. Wierzbicki, *On fracture locus in the equivalent strain and stress triaxiality space*, International Journal of Mechanical Sciences, Vol. 46, 2004, pp.81-98.

[35] H. Kolsky, *Stress Waves in Solids*, Dover Publication, New York, 1963.

[36] N.A. Fellows and J. Harding, *Localization of plastic deformation during high strain rate torsion testing of rolled homogeneous armour*, Journal of Strain Analysis, Vol. 36, No. 2, 2001, pp 197-210.

[37] S.-C. Liao and J. Duffy, *Adiabatic shear bands in a Ti-6Al-4V titanium alloy*, J. Mech. Phys. Solids, Vol 46, No 11, 1998, pp.2201-2231.

[38] K.A. Hartley, J. Duffy and R.H. Hawley, *Measurement of the temperature profile during shear band formation in steels deforming at high strain rates*, J. Mech. Phys. Solids, Vol. 35, No. 3, 1987, pp. 283-301.

[39] V.A. Fedorchuk, *Localization of plastic shear under impact loading*, Stength of Materials, Vol. 34, No. 3, 2002, pp. 256-258.

[40] C. Mason and M.J. Worswick, *Adiabatic shear in annealed and shock hardened iron and in quenched and tempered 4340 stell*, International Journal of Fracture, Vol. 111, 2001, pp. 29-51.

[41] C.E. Franz, P.S. Follansbee, and W.E. Wright, *New experimental techniques with the Split Hopkinson Pressure Bar*, High Energy Rate Forming, ASME, 1984.

[42] Z. Rosenberg, D. Dawicke, E. Strader, S.J. Bless, *A new technique for heating specimens in split Hopkinson bar experiments using induction-coil heaters*, Experimental Mechanics, Vol. 26, No. 2, 1986, pp. 275-278.

[43] M. Shazly, D. Nathenson, and V. Prakash, *Modeling of high-strain-rate deformation, fracture, and impact behavior of advanced gas turbine engine materials at low and elevated temperatures*, NASA/CR-2003-212194, 2003.

[44] A. Gilat, X. Wu, *Elevated temperature testing with the torsional split Hopkinson bar*, Experimental Mechanics, Vol. 34, No. 2, 1994, pp.166-170.

[45] Manual No. 10-1137-1, *Instron 1137 operating manual*, p.2-1.

[46] I. Rohr, H. Nahme, K. Thomas, Charakterisierung des Schaedigungsverhaltens von duktilem Stahl, Frauhnofer Enrst-Mach-Institut, 79104 Freiburg.

Appendix A

Tensile test specimen technical draw

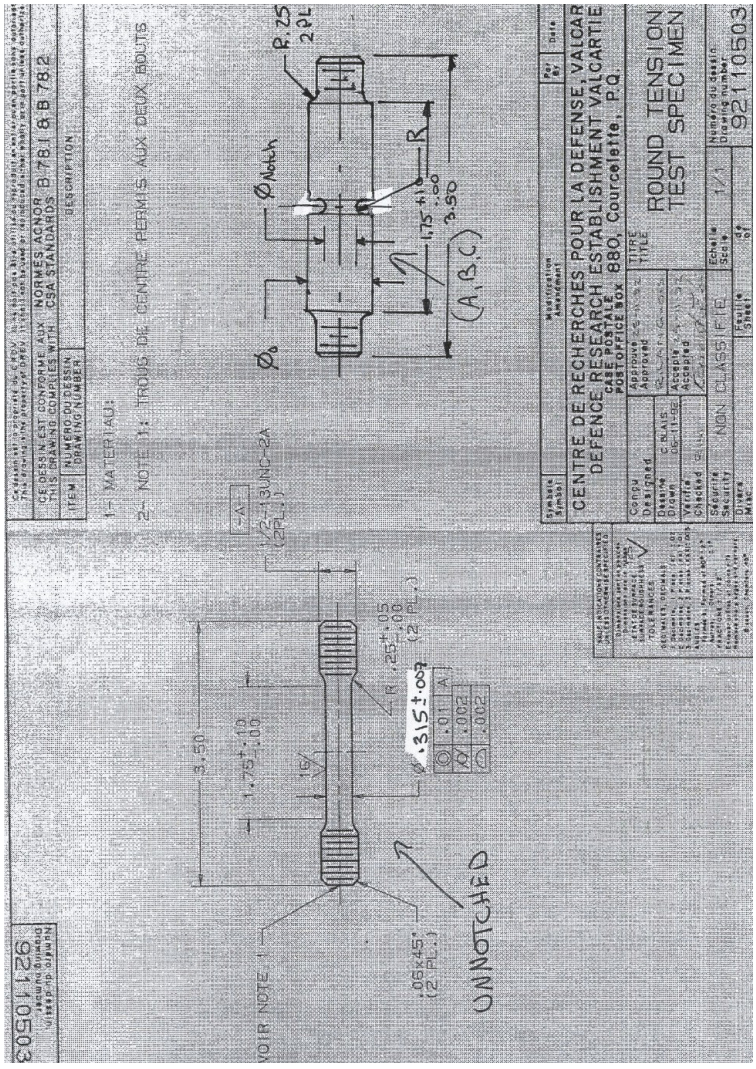

Figure A.1: Technical draft of the tensile test's specimens.

Appendix B

Tensile tests results

Table B.1: Tensile test's results on RHA steel 4043

Specimens	Srewdriven head speed (mm/min)	Load max (kN)	Elongation on 25.4mm (%)	Area reduction (%)	Strain to fracture (%)
RHAUN01	10	59.08	19.8	64.7	104.3
RHAUN02	10	60.03	20.1	60.5	92.8
RHAUN03	10	59.58	20.2	64.3	103.0
RHAUN04	2		21.2	62.6	98.4
RHAUN05	2	59.93	21.2	61.6	95.6
RHAUN06	2	59.68	21.8	62.0	96.8
Note: Specimens RHAUN07-08 were tested without strain gage.					
RHAUN07	2	59.44		64.2	102.6
RHAUN08	2	59.81		61.7	96.0
RHA12mm01	2	69.24	-	45.2	60.2
RHA12mm02	2	69.36	-	43.4	56.8
RHA12mm03	2	69.98	-	39.7	50.6
RHA12mm04*	2	60.21	-	22.7	61.2
*Initial specimen's radius at notch: $7.55mm$					
RHA6mm01	2	74.23	-	36.8	45.9
RHA6mm02	2	75.13	-	31.5	37.9
RHA6mm03	2	74.33	-	37.2	46.5
RHA6mm04	2	76.24	-	31.0	36.1
RHA4mm01	2	79.60	-	31.1	37.3
RHA4mm02	2	79.52	-	26.9	31.3
RHA4mm03	2	80.00	-	26.5	30.7
RHA4mm04	2	79.34	-	26.8	29.9